Express Polymer Letters Vol.16, No.9 (2022) 939–959
Available online at www.expresspolymlett.com
https://doi.org/10.3144/expresspolymlett.2022.69

Research article

Synthesis and characterization of new nanocomposites of [poly(*o*-toluidine)]/(WO_3 nanoparticles) and their application in novel hybrid solar cells

Edris Valadbeigi[1], *Ali Reza Modarresi-Alam*[1,2*], *Meissam Noroozifar*[3], *Ali Reza Rezvani*[4]

[1]Organic and Polymer Research Laboratory, Department of Chemistry, Faculty of Science, University of Sistan and Baluchestan, Zahedan, Iran
[2]Renewable Energies Research Institute, University of Sistan and Baluchestan, Zahedan, Iran
[3]Department of Physical and Environmental Sciences, University of Toronto Scarborough, 1265 Military Trail, M1C 1A4 Toronto, ON, Canada
[4]Inorganic Laboratory, Department of Chemistry, Faculty of Science, University of Sistan and Baluchestan, Zahedan, Iran

Received 26 November 2021; accepted in revised form 15 May 2022

Abstract. The derivatives of polyaniline have obtained remarkable attention due to their electronic applications in the field of nanomaterials. This work considers the electronic, structural, and photovoltaic properties of nanocomposites (POT/WO_3NPs) synthesized with three different ratios of poly(*o*-toluidine) and WO_3 nanoparticles [*a-c* ($mol_{WO3}/mol_{monomer}$) 100 = 60, 65, 70%] using a template-free method and a basic mechanochemical reaction in solid-state. The nanocomposites are analyzed and characterized by various spectroscopy methods. The prepared nanocomposites have core-shell morphology. The results of the band gap assessed *via* cyclic voltammetry and UV-vis specified that the forbidden band gap for (POT/WO_3NPs) nanocomposite *b* [($mol_{WO3}/mol_{monomer}$) 100 = 65%] are about 1.03 and 1.5–1.9 eV, respectively. The *J*–V analysis and power conversion efficiency of the fabricated devices FTO|TiO_2NPs|POT|Al and FTO|TiO_2NPs|POT/WO_3NPs (*a-c*) |Al single-layer solar cells are performed and discussed. The photovoltaic energy conversion efficiency (PCE) of the two devices are 0.18% and in average, 0.57%, respectively. The data show both indirect and direct transitions are observed for the WO_3NPs, POT, and POT/WO_3NP (*b*). This investigation demonstrates that the morphology and architecture of nanocomposites (POT/WO_3NPs) can be helpful in improving solar cell performance.

Keywords: *nanocomposites, conductive polymers, hybrid solar cell, mechanochemical reaction, poly(o-toluidine)*

1. Introduction

Substituting fossil fuels with renewable energy sources is considered the most important challenge of the 21st century. By enhancing the population, the energy requirement is sharply enhanced. To this end, solar energy can be assumed as one of the potential alternatives to meet this enhancing energy requirement. Due to the fact that CO_2 is generated by fossil fuels which leads to the greenhouse effect, solar energy has obtained considerable attention because of being clean. Moreover, environment and energy are nowadays known as the hottest topics [1–5] and have attracted many researchers worldwide to follow and develop different sustainable and renewable sources. Inorganic-organic hybrid nanomaterials commonly play an important role in extending materials with great efficiency and functionality [6]. The hybrid nanomaterials are expected to show the benefits of both inorganic and organic materials. Moreover, hybrid nanomaterials can also have new attributes that are not seen in the inorganic and organic nanomaterials independently. Therefore, inorganic-organic

*Corresponding author, e-mail: modaresi@chem.usb.ac.ir

hybrid nanomaterials have obtained considerable attention from materials scientists, chemists, physicists, and engineers to use their significant applications in various fields like sensors, mechanics, energy, catalysts, optical, and electronic tools [6]. In this regard, polyaniline (PANI) is known as one of the most used and investigated polymers among different intrinsically conductive polymers due to its distinctive non-redox doping/de-doping chemistry, environmental stability, high conductivity, optical, and electrochemical attributes [7–23]. Recently, inorganic compounds and PANI nanocomposites were fabricated to provide new materials with improved attributes [24–30].

Poly(*o*-toluidine) [POT] is a polyaniline derivative that has the methyl group in its *ortho* position. In recent years, POT has also presented additional benefits considering the PANI owing to its shorter switching time between the oxidized and reduced states [31–33]. Compared to the electrochemical technique, PANI chemical fabrication is extensively employed for mass production [34]. Different kinds of oxidants like $(NH_4)_2S_2O_8$ [34–37], $FeCl_3$ [38, 39], $K_2Cr_2O_7$ [37, 40] and H_2O_2 [37] can be utilized in the PANI chemical fabrication. Apart from the traditional TiO_2, ZnO, and WO_3 as binary oxides, they are also presented to be effective as photocatalysts in various processes. The WO_3 is most investigated among different inorganic materials due to its remarkable benefits like great chemical stability, original color switching, and powerful adherence to the substrate [41–45].

WO_3 has been efficiently used in various electrochromic tools, photo electrocatalytic processes, dye-sensitized solar cells, and gas sensors. In spite of the fact that the combination has presented some great benefits, WO_3/PANI composites, which are mostly reported, are in a two-dimensional shape while their lateral size is about several micrometers [46–50]. Furthermore, the nanostructured composites presented efficient electrical, mechanical, and optical attributes provided by restricting such materials' dimensions and synthesizing the surface and bulk attributes to the final behavior. The possible capacity of materials with decreased dimensions becomes interesting in various feasible applications. The inorganic moieties' stability can be enhanced via inorganic-organic interactions [51, 52].

Conducting polymers can also be considered suitable candidates for inorganic materials stabilization. Many studies about conducting polymer according to inorganic-organic hybrid materials, like V_2O_5/PANI [53], MWNT/Fe_3O_4/PANI [54], MnO_x/PANI [55], and TiO_2NPs/PANI [56], have been recently conducted. Following a similar line of research, a template-free and simple solid-state mechanochemical reaction were utilized to fabricate poly(*o*-toluidine)/tungsten trioxide nanoparticles (POT/WO_3NPs) nanocomposites *a-c* [$(mol_{WO_3}/mol_{monomer})\cdot 100 = 60$, 65, 70%] in this paper for the first time aiming to study morphology, molecular structure, important optical attributes, and nanocomposites electronical behavior. Transmission electron microscope (TEM), Fourier transform infrared (FT-IR), X-ray diffraction (XRD), thermal gravimetric analysis (TGA), field emission scanning electron microscope (FE-SEM), and elemental analysis (CHN) were used to investigate the morphological and molecular structures of the sample. Cyclic voltammetry (CV) and (UV-vis) photo spectrometers were respectively utilized to verify the electrical and optical attributes of the samples.

Then, single-layer hybrid solar cells were designed as FTO|TiO_2NPs|POT|Al and FTO|TiO_2NPs|POT/WO_3NPs *a-c* |Al. Noteworthy, this is the first time that POT/WO_3NPs *a-c* are utilized in the hybrid solar cell of the solid-state. The photocell properties like short circuit current (J_{SC}), open-circuit voltage (V_{OC}), energy conversion efficiency (η), and fill factor (*FF*) were computed in the condition under simulated sunshine light (100 $mW\cdot cm^{-2}$ irradiation and AM 1.5 global conditions). The assessment of the synthesized hybrid solar cell was found to be near the energy permutation efficiency in average of 0.57% with a small gap of energy.

2. Experimental

2.1. Materials and instrumentation

Iron (III) chloride hexahydrate ($FeCl_3\cdot 6H_2O$) and *o*-toluidine (99%) Merck (Darmstadt, Germany) were utilized without purification. TiO_2 paste created from TiO_2NPs < 20 nm (PST-20T) Merck (Darmstadt, Germany). The aluminum foil (70 μm thickness) was bought from Sharif Solar Technology Development Company (Tehran, Iran). Conductive fluorine-doped tin oxide (FTO) coated on glasses with dimensions of 15 to 20 mm (thickness of 585 nm) and lower sheet resistance than 10 $Ohm\cdot sq^{-1}$ were bought from Xinyan Technology Co. (Hong Kong, China).

The one-sixth of FTO length with the above dimensions was eliminated by etching with Zn and HCl

1 M. In the next step; the substrates were cleaned in an ultrasonic tank containing soap, acetone, ethyl alcohol, and distilled water (DW), respectively, in sequence for 15 minutes [56–60].

FT-IR spectrophotometer (JASCO spectrum 2000, Madison, USA) utilizing KBr compact tablets was employed to record the FT-IR spectra of the powdered materials in the range of 500 to 4000 cm^{-1} TEM (Philips, EM208 S, Amsterdam, Netherlands) and FE-SEM (MIRA3TESCAN-XMU, Brno, Czech Republic) were also used to analyze the synthesized and purchased samples' morphologies. Cyclic voltammetry (CV) was also employed to explore the oxidation and reduction processes conducted by the glassy carbon electrode (GCE) in 1.0 M sulfuric acid (SAMA-500, SAMA Research Center, Isfahan, Iran). FTO conductive glass as a working electrode was used to record the diagrammatic curves of cyclic voltammetry for specifying the samples' band gap, and therefore the samples were coated on it. Platinum rod and Ag/AgCl were respectively selected as the auxiliary and reference electrodes. $(n\text{-}Bu)_4NClO_4$ (0.1 M) dissolved in the CH_3CN solvent was also considered as the electrolyte solution. The process was conducted under an N_2 atmosphere while the temperature was about 25 °C at very slow potential sweep rates (0.1 $V \cdot s^{-1}$).

The crystal nature of the fabricated nanocomposites was analyzed by X-ray powder diffraction (Mini Materials Analyzer (MMA), GBC Scientific Equipment, Braeside, VIC, Australia) at 35.4 kV and 28 mA. The 2θ scanning range was set between 10 and 80° at a scan rate of 0.05° $\cdot s^{-1}$). A PG UV-vis spectrophotometer (models: $T80^+$ instrument Ltd., Tokyo, Japan) was used to measure ultraviolet-visible (UV-vis) absorbance spectra that were in the range of 200 to 1100 nm by dissolving the samples in formic acid. Current-voltage (J-V) attributes were examined on simulated solar (IRASOL, SIM-1000, Tehran, Iran) under 100 $mW \cdot cm^{-2}$ irradiation and 1.5 AM global conditions. A calibrated photodiode (Thorlabs, 50 $mV \cdot s^{-1}$) was also used to monitor the illumination intensity. A D conventional 4-probe device was utilized to record the electrical conductivity (EC) of the samples as bulk tablets (no film) (Zahedan, Iran).

2.2. Synthesis of tungsten trioxide nanoparticles (WO_3NPs)

The precipitation method, explained by Supothina *et al*. [61], was used to synthesize WO_3 nanoparticles. According to the mentioned process, 1.07 mmol of ammonium tungstate hydrate ($H_{42}N_{10}O_{42}W_{12} \cdot xH_2O$) was dissolved under continual stirring in distilled water (67 ml) while the temperature was about 80 °C. After complete dissolution, 45 ml of concentrated nitric acid (HNO_3 65%) was dropwise poured into the tungstate solution. In the following, the mixture was held at 80 °C for 50 min with a controlled continual stirring (800 rpm). Thereafter, the precipitates were permitted to become settled for 1 day at room temperature (*RT*). The aqueous solution was decanted, and the DW was included with continual stirring. The precipitates' sedimentation process was then done again. An oven with a temperature of 80 °C was employed to dry the precipitates [62].

2.3. Synthesis of poly(*ortho*-toluidine) (POT)

The POT was synthesized based on the following steps: 0.428 g (4 mmol) *o*-toluidine and 2.70 g (10 mmol) $FeCl_3 \cdot 6H_2O$ were each hand-ground lightly for 5 minutes in a particular large ceramic mortar (to be completely powdered) then they were mixed, and the grinding continued. The initial color of the mixture was orange, which was owing to the $FeCl_3 \cdot 6H_2O$. In the following, the mixed powders mode was turned to the sludge after 15 minutes of grinding (the temperature was between 25–30 °C). The color of the slurry was turned green by continuous grinding. Due to the presence of chlorine and hydrogen ions, along with the mechanochemical reaction, the acidic environment led to the Fe^{3+} reduction and doped POT production in the form of emeraldine salt (ES). After grinding for another 1 hour, the product was achieved. Purification and filtration were respectively performed by adding deionized water and rinsing with 20 ml of deionized water (two times) using a Buchner funnel (under vacuum by aspirator) [56, 63–66].

2.4. The nanocomposites synthesis of poly(*ortho*-toluidine)/tungsten trioxide nanoparticles (POT/WO_3NPs) *a-c* in different ratios of POT and WO_3NPs

The poly(*o*-toluidine)/(WO_3 nanoparticles) nanocomposites *a-c* were fabricated based on the novel synthetic method presented in Figure 1. The POT/WO_3NPs nanocomposites *a-c* were synthesized in different ratios of POT and WO_3NPs [$(mol_{WO_3}/mol_{monomer}) \cdot 100$ = 60, 65, 70%] with a mechanochemical method, similar to the above-mentioned method for poly(*o*-toluidine). In a typical

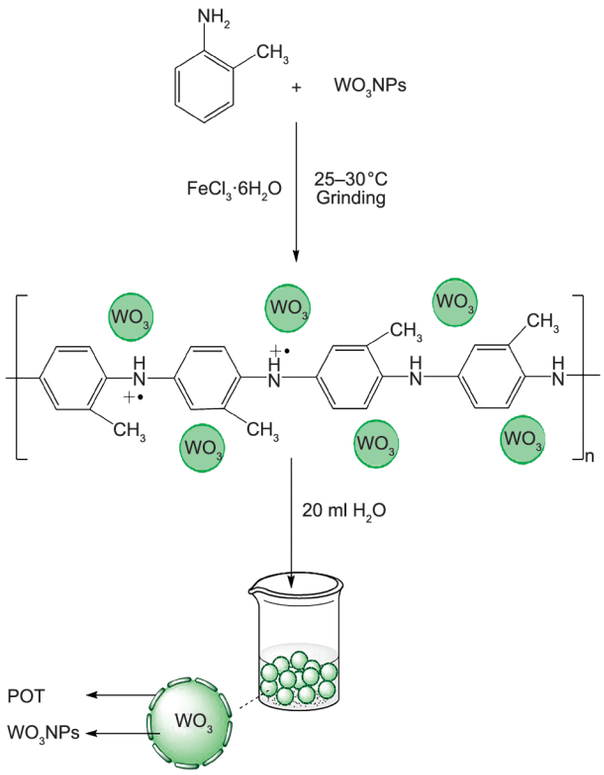

Figure 1. Schematic representation of the synthesis of core-shell nanocomposites **a-c** (POT/WO_3NPs).

procedure, nanocomposite *b* [(mol_{WO_3}/$mol_{monomer}$) ·100 = 65%]: first, 0.428 g (4 mmol) of *o*-toluidine with (0.625 g, 2.7 mmol) of WO_3 nanoparticles were lightly hand-grounded for 5 minutes inside a large ceramic mortar. Afterward, 2.70 g (10 mmol) of $FeCl_3 \cdot 6H_2O$, as an oxidant, was put into the mix to perform an oxidative polymerization of the monomer. The color of the mixed powders mode was altered to the slurry after 15 minutes of grinding while the temperature was in the range of 25 to 35 °C. The reaction was perused with the grinding, and the color of the mixture was finally turned green from orange, demonstrating the process of polymerization. Later than grinding slurry for another 1 hour, DW (20 ml) was added to the desired product, and then a Buchner funnel was used to slowly filter the obtained product [56, 63–66].

Nanocomposites *a* and *c* were prepared similar to the above-explained procedure with [(mol_{WO_3}/$mol_{monomer}$)·100] 60% and 70%, respectively.

Since there is no considerable change in results obtained from FT-IR, XRD, FE-SEM, and their performance in the photovoltaic cells, we here just consider nanocomposite *b* [(mol_{WO_3}/$mol_{monomer}$)·100 = 65%].

2.5. Fabrication of FTO|TiO_2NPs|POT|Al and FTO|TiO_2NPs|POT/WO_3NPs *a-c* |Al solar cells

The architecture of FTO|TiO_2NPs|POT|Al and FTO|TiO_2NPs|POT/WO_3NPs *a-c* |Al were afterward obtained by doctor blade methods [67]. The thin coating of standard transparent TiO_2NPs paste was created using TiO_2 nanoparticles on an FTO coated on glass by the doctor blade. The film was sintered in the kiln based on the program reported in the TiO_2NPs paste catalog [68]. A suitable amount of POT/WO_3NPs *a-c* were poured into *N*-methyl-2-pyrrolidone (NMP) and was then exposed to ultrasonic irradiation for 10 min to achieve good dispersion. Then, it was injected between FTO|TiO_2NPs substrate and aluminum foil, in the form of a sandwich-type cell which was kept on hand at the least pressure, and then the tools were fixed by binder clips 18 mm. These architectures are shown in Figure 10. The cell dimension for these analyses was 1 cm^2. The I–V evaluation was done utilizing the simulated solar irradiation under global AM 1.5.

3. Results and discussion

3.1. FT-IR spectra

The FT-IR measurements on WO_3NPs, POT, and POT/WO_3NPs *b* hybrid nanocomposite were conducted, and the results are illustrated in Figure 2. Since there is no considerable change in results

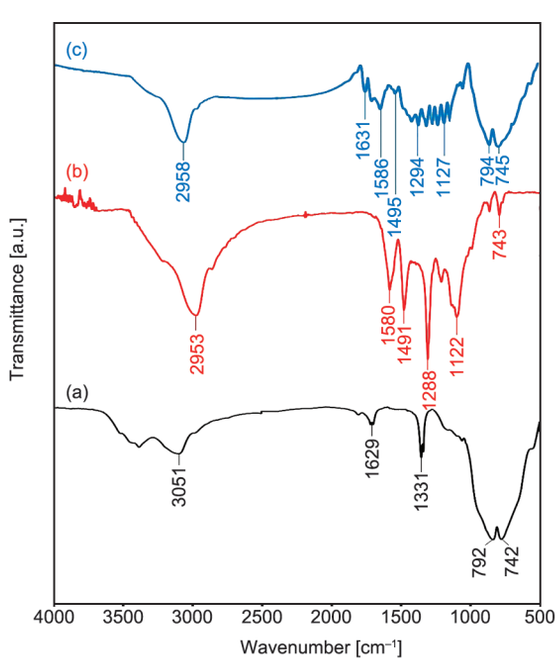

Figure 2. The FT-IR spectra of WO_3NPs, POT, and POT/WO_3NPs *b*.

obtained from FT-IR spectra of nanocomposite a and *c*, we here just consider nanocomposite *b* [($mol_{WO_3}/mol_{monomer}$)·100 = 65%].

According to the FT-IR spectrum of WO_3NPs, the bands at 742 and 792 cm^{-1} are related to the stretching vibrations of W=O bands and the bridging oxygen of W–O–W bands in WO_3NPs [69]. In fact, the peak at 1629 cm^{-1} is ascribed to the OH bending vibrations mixed with tungsten (W) atoms. The broad peak located at 3051 cm^{-1} is owing to the OH group on the WO_3 surface [70]. In the FT-IR spectrum of POT, the peak that appeared at 743 cm^{-1} is mostly attributed to C–H bending vibration (out of plane) of the benzene ring [71]. The peaks at 1288 and 1122 cm^{-1} are respectively related to the C–N stretching and C–H bending vibrations of the secondary aromatic amine [72]. The FT-IR peaks centered at 1580 and 1491 cm^{-1} are respectively attributed to the C=N and C=C stretching mode of the quinoid rings and the C=C stretching mode of benzenoid rings [73].

FT-IR spectrum of POT/WO_3 *b* confirming the impact of synthesis of WO_3NPs on chemical interactions of the mixed nanocomposite is illustrated in Figure 2. The peak at 2958 cm^{-1} may be related to the CH_3 stretching vibration in methyl groups [74]. The remarkable alteration in the FT-IR spectrum of POT/WO_3 *b* is related to the interaction of hydrogen bondings between WO_3NPs and the N–H groups in the POT chains. Accordingly, it can be suggested that the W in WO_3NPs has a severe propensity to create coordination sites with the –N– atoms in POT chains that can result in an alternation of distribution of the electron density [75].

3.2. UV-vis spectroscopy

The WO_3NPs, POT, and POT/WO_3NPs *b* were dissolved in NMP and formic acid to evaluate the optical characteristics (Figure 3, and Table 1). These also display which three particular peaks of doped POT emerged around 343, 431, and 795 nm are respectively ascribed to the π–π^*, polaron–π^*, and π–polaron transition [76–78]. POT/WO_3NPs *b* shows the basic specific peaks of WO_3NPs and doped POT that all appeared in POT/WO_3NPs while a new peak is also seen at 250 nm. The fundamental indirect allowed transitions of WO_3 are due to the transition from O2p electrons from the valence band to the W5d conduction band. The exact location of this band maximum depends on the extent of distortion of the isolated WO_4 structure [79].

Additionally, the peak centered at 795 nm is shifted to 800 nm [80, 81]. These alternations can be related to the existence of WO_3NPs. Moreover, it is clear that WO_3NPs encapsulation also has an effective impact on the doping of conducting POT which can be due to an interaction at the junction of POT and WO_3NPs.

Two distinctive absorption peaks at 328 and 560 nm were observed in the NMP solvent. The former is attributed to the $\pi \rightarrow \pi^*$ electron transition of the benzenoid ring, and the latter is the $n \rightarrow \pi^*$ transition of benzenoid to quinoid [56, 82–88]. Indeed, the nanocomposite is red-colored in NMP solvent. The absorption at 560 nm is influenced by the oxidation state of the molecules. This result shows that POT/WO_3NPs is completely transformed from the emeraldine salt to the emeraldine base by the deprotonation of POT/WO_3NPs *b* by NMP. It is known that a strong hydrogen bond can be formed between the $–NH^{+\bullet}–$ and/or $=NH^{+}–$ sites in the polymer backbone and the carbonyl group of NMP, which leads to deprotonation of the polymer backbone of POT and conversion of emeraldine salt to emeraldine base [80–88]. The color-changing from green to blue can also be evidence of these events. On the other hand, according to the peak position of polymer and the nanocomposite, the nanocomposite has a red shift compared to POT, indicating that the nanocomposite is successfully synthesized.

In inorganic and organic molecules, the electronic states' energy levels are related to the energy obtained via visible or UV irradiation. On the other hand, quantified energy transferred via electromagnetic rays can be absorbed by the materials at resonance and move an electron from the lower energy level to a higher energy level [89]. UV-vis absorption spectra can be used to evaluate these transitions. E_{opt} is related to the long-wavelength edge energy of the exciton absorption band [88, 90]. The longest absorption wavelength λ_{onset} is utilized to specify the optical gap energy (E_g^{Opt}) according to Equation (1) [91, 92]:

$$E_g^{Opt} = \frac{1242}{\lambda_{onset\,[nm]}} \tag{1}$$

Based on the existing spectra, the absorption edge of each sample was determined. The plot of $(\alpha h\upsilon)^2$

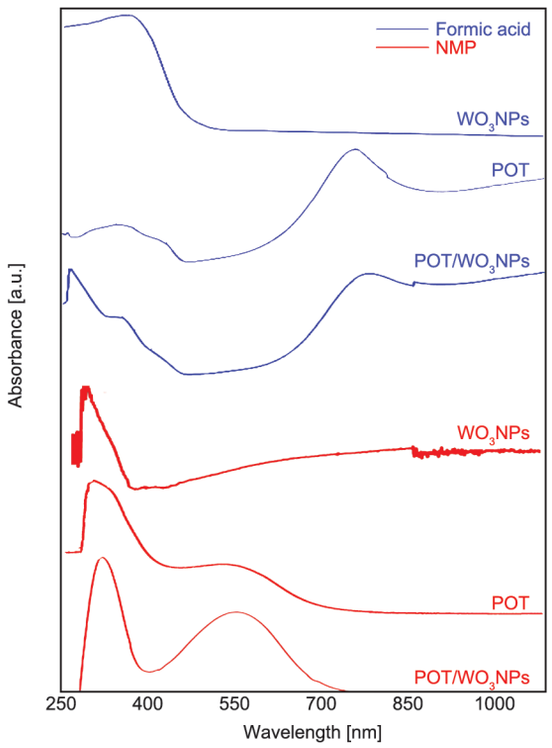

Figure 3. UV-vis spectra of WO_3NPs, POT and POT/WO_3NPs *b* in formic acid (0.02 $g \cdot l^{-1}$) and in NMP (0.02 $g \cdot l^{-1}$).

[$eV^2 \cdot cm^{-2}$] *vs.* photon energy [eV] and $(\alpha h\upsilon)^{1/2}$ [$eV^{1/2} \cdot cm^{-2}$] *vs.* photon energy [eV] are used to extract absorbance data (Table 1) [93–97]. The absorption edge [nm] and optical E_g [eV] of WO_3NPs, POT, and POT/WO_3NPs *b* are presented in Table 1. UV-vis and FT-IR spectra analysis strictly present a possibility of electrochemical stability enhancement due to the interaction between POT and WO_3NPs.

To estimate the optical band gap (E_g^{Opt}) of the WO_3NPs, POT, and POT/WO_3NPs *b*, a plot of $(\alpha h\upsilon)^n$ against $h\upsilon$ [93–97] is done in two solvents FA and NMP, respectively. The *n* factor depends on the nature of the electron transition and is equal to 2 or 1/2 for the direct and indirect transition band gaps, respectively [93–97]. Both curves $(\alpha h\upsilon)^{1/2}$ against $h\upsilon$ and $(\alpha h\upsilon)^2$ against hυ were plotted. The plot of $(\alpha h\upsilon)^{1/2}$ against $h\upsilon$ (indirect transition) had a better fit but a little less amount in the obtained band gap. All the data are reported in Table 1.

For the WO_3NPs, POT, and POT/WO_3NPs *b* in FA solvent, only one E_g^{Opt} was observed in two plots which are attributed to transfers of polaron→π^*. In FA, since this solvent acts as a dopant (protic solvent) and causes the formation of polarons and bipolarons due to the complete doping process [80], only one E_g^{Opt} was observed, which is attributed to transfers of polaron→π^*. Usually, a direct transition band gap was observed for PANI derivatives and their composites [98–100]. However, both indirect and direct band gaps were reported for the WO_3 [47, 100–103]. Both indirect and direct transitions were observed for the WO_3NPs, POT, and POT/WO_3NPs *b*, with a better fit but a little less amount in the indirect band gap.

Although an indirect semiconductor absorbs light poorly, it generally possesses a large recombination lifetime and hence a large diffusion length. Because the diffusion length roughly scales inversely to the absorption strength of a pure semiconductor, there is no real disadvantage in using an indirect gap semiconductor, just as long as the absorbing layer is thick enough [93–98].

For this reason, the indirect band gap shows the contradiction between the long charge carrier lifetime and strong absorption.

In semiconductors with direct band gap, the electronic transition from VB to CB is electrical dipole permitted and the electronic absorption, as well as emission, is typically strong. In semiconductors with indirect band gap, VB to CB electronic transition is forbidden in terms of the electrical dipole, and the transition is phonon-assisted, *i.e.*, both momentum and energy of the electron-hole pair are altered in the transition. Both their absorption and emission are

Table 1. Absorption edge [nm] and band gap energy for WO_3NPs, POT, and POT/WO_3NPs *b*. Direct and indirect band gaps were obtained in two solvents, FA and NMP.

Compound	Assignments	Absorption edge [nm]	E_g [by the plot of $(\alpha h\upsilon)^n$ *vs.* $h\upsilon$] [eV]			
			Direct band gap	Indirect band gap	Direct band gap	Indirect band gap
WO_3NPs	O2p (VB)→W5d (CB)	321	2.77	2.87	2.68	2.18
POT	polaron→π^*	431	2.64	2.78	1.96[a] and 3.29[b]	1.78[a] and 2.12[b]
POT/WO_3NPs *b*	polaron→π^*	412	1.82	1.98	1.90[a] and 3.32[b]	1.59[a] and 2.90[b]

[a]n→π^*
[b]π→π^*

weaker in comparison to those of semiconductors with direct band gap because they involve a change in momentum.

Interactions among photons, holes, electrons, phonons and other particles are needed to satisfy the conservation of energy and crystal momentum (*i.e.*, conservation of total *k*-vector). Afterward, the nature and origin of the electronic transitions remain quite uncertain and are expected to depend on the interactions between the individual components of the composites, pressure, temperature, morphology, and so on [93–98].

For example, since at low temperatures, there are fewer phonons, and thus it is less probably that a phonon and photon can be concurrently absorbed to generate an indirect transition, and then, low temperatures are for the benefit of indirect transition. Also, it was demonstrated that the band gap changed with pressure, and the direct transition was enhanced [97].

3.3. Cyclic voltammetry

Figure 4 demonstrates the CV curves obtained at WO_3NPs, POT, and POT/WO_3NPs *b* by GCE in 1.0 M of sulfuric acid over the potential window ranging from –1.0 to 1.0 V (*vs*. Ag/AgCl) at a sweep rate of (0.1 $V \cdot s^{-1}$). WO_3 revealed a broad oxidative hump, which can be ascribed to the de-intercalation of intercalated protons from WO_3NPs. The mentioned process can be described as Equation (2):

$$WO_3 + xH^+ + xe^- \rightarrow H_xWO_3 \quad (2)$$

Further consideration shows three redox pairs emerged at POT/WO_3NPs . The redox couples A/A′ and C/C′ originate from the transitions between the leucoemeraldine/emeraldine and emeraldine/pernigranilin states of POT, respectively (see Equations (3) and (4)). The redox couple labeled as B/B′ is assigned to the intercalation of the proton on WO_3 [104]. The chemical structures corresponding to oxidation/reduction transitions of POT are illustrated as:

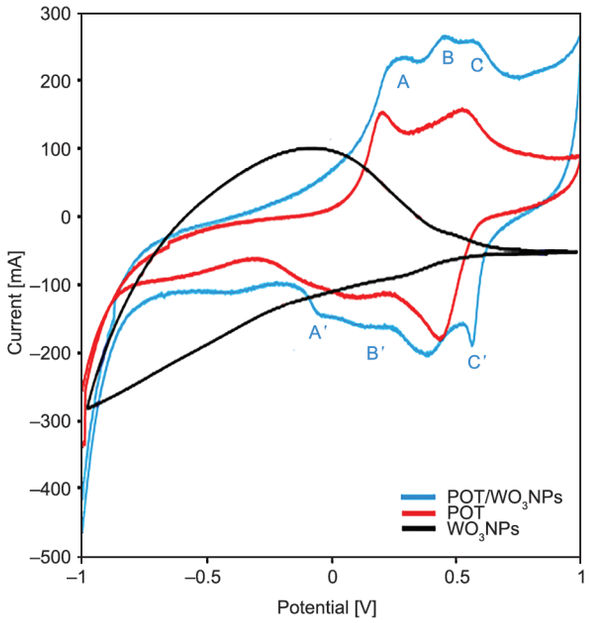

Figure 4. Cyclic voltammograms obtained at WO_3NPs, POT, and POT/WO_3NPs *b* in a solution of 1.0 M sulfuric acid at a scan rate of 0.1 $V \cdot s^{-1}$.

3.4. Band gaps (E_g), HOMO, and LUMO energies

FTO conductive glass was utilized as a working electrode to record the cyclic voltammetry diagrams to achieve the electrochemical data. Platinum rod and Ag/AgCl were respectively selected as the counter and reference electrode. $(n\text{-}Bu)_4NClO_4$ (0.1 M) dissolved in the CH_3CN solvent was chosen as the electrolyte solution. The process was conducted under an N_2 atmosphere at very slow potential sweep rates (0.1 $V \cdot s^{-1}$) while the temperature was also about 25 °C. The levels of energy were specified toward the standard hydrogen electrode (SHE) by an amount of 4.4 eV and based on the level of vacuum that is assumed as zero [105–107]. The results of the experiments are presented in Figure 5, while Table 2 includes the summary of the computed data. The electrochemical band gap energy (E_g^{CV}) of the POT, WO_3NPs, and POT/WO_3NPs *b* were achieved from analysis of their CV curves. Firstly, the energy levels

LS $\rightleftharpoons$ ES:

$$\underset{\text{Leucoemeraldine (yellow)}}{\text{POT-LM}} + 2nHSO_4^- \rightarrow \underset{\text{Emeraldine-salt (green)}}{(\text{POT-ES})^{2n+}(HSO_4^-)_{2n}} + 2ne^- \quad (3)$$

ES $\rightleftharpoons$ PS:

$$\underset{\text{Emeraldine-salt (green)}}{(\text{POT-ES})^{2n+}(HSO_4^-)_{2n}} + 2nHSO_4^- \rightarrow \underset{\text{Pernigranilin-salt (purple)}}{(\text{POT-PS})^{4n+}(HSO_4^-)_{4n}} + 2ne^- \quad (4)$$

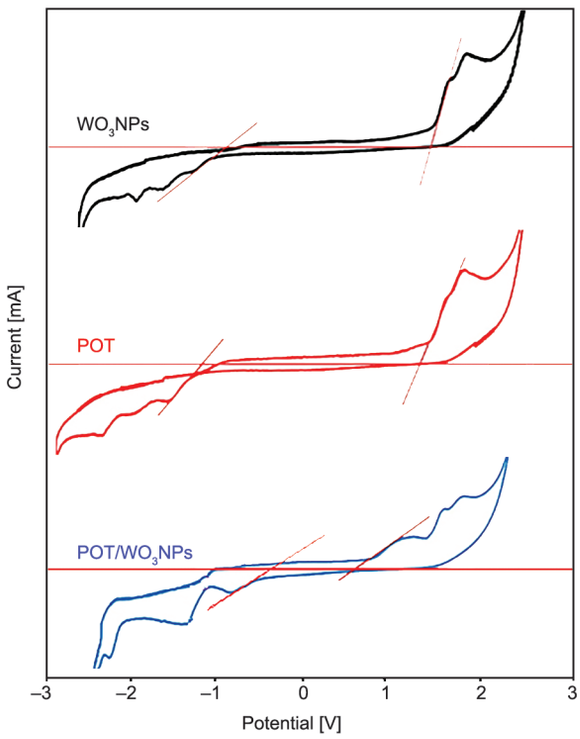

Figure 5. Cyclic voltammogram of WO_3NPs, POT, and POT/WO_3NPs *b* in Bu_4NClO_4 (0.1 M) of CH_3CN solution at a scan rate of (0.1 $V \cdot s^{-1}$) under an N_2 atmosphere.

of the lowest unoccupied molecular orbital (LUMO) and the highest occupied molecular orbital (HOMO) were respectively computed using the reduction and oxidation potential values (Equations (5) and (6)). Thereafter, the energy (E_g^{CV}) was computed using the discrepancy of the HOMO and LUMO energy levels based on Equation (7) [107–109].

$$E_{HOMO} = -(E_{onset}^{Ox} + 4.44)\ [eV] \quad (5)$$

$$E_{LUMO} = -(E_{onset}^{Red} + 4.44)\ [eV] \quad (6)$$

$$E_g^{CV} = -(E_{HOMO} - E_{LUMO})\ [eV] \quad (7)$$

It can be said that when POT is in the form of emeraldine salt (ES), the LUMO and HOMO energy levels

Table 2. The molecular orbitals energy level and energy gap of WO_3NPs, POT, and POT/WO_3NPs *b*.

Sample	Onset oxidation potential [eV]	Onset reduction potential [eV]	E_{HOMO} [eV]	E_{LUMO} [eV]	(E_g^{CV}) [eV]
WO_3NPs	1.69	–0.91	–6.13	–3.53	2.60
POT	1.40	–1.12	–5.84	–3.32	2.52
POT/WO_3NPs *b*	0.68	–0.35	–5.12	–4.09	1.03

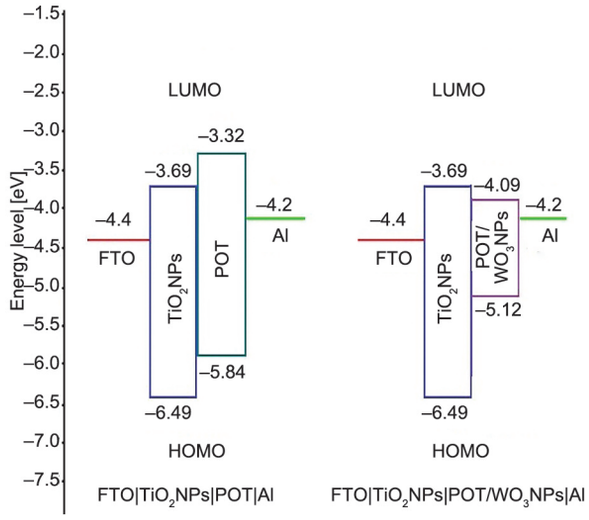

Figure 6. Energy band diagram of WO_3NPs, POT, and POT/WO_3NPs *b*.

of POT are respectively relevant to the π^* energy level in CB and the polaron band [110, 111]. Figure 6 presents the comparison of the HOMO, LUMO levels, and gap energies (E_g^{CV}) of POT, WO_3NPs, and POT/WO_3NPs *b* as an energy band diagram (at a glance). The band gap (E_g^{CV}) of WO_3NPs, POT, and POT/WO_3NPs b were respectively about 2.60, 2.52, and 1.03 eV.

Based on the obtained results, POT/WO_3NPs *b* is a P-N type of hoping the material. Comparing (E_g^{CV}) with an optical band gap energy (E_g^{Opt}) of samples indicated that there is a low discrepancy between them. The oxidation and reduction process that takes place in a separated electron and hole transporting units (not in a completely conjugated system) can be considered the first reason [107].

Moreover, UV-vis spectra were conducted in solution while CVs were recorded in solid-state can be stated as the second and more significant reason. However, some of the POT chains take off from the surface of WO_3NPs in solution, and next, they are separated from one another. As a matter of fact, although POT chains have almost identical chemical forms, their organization in solution and solid-state is different. In this regard, the polymer chains in solid-state have a considerably expanded coil conformation while in solution have a compacted coil conformation owing to the great chains' flexibility [32, 50, 112–114]. In fact, POT chains generally have a rigid interaction with each other and with WO_3NPs as the main nanocomposite components in the solid state. Finally, a greatly expanded coil conformation is provided for POT chains using these interactions.

3.5. Analysis of X-ray diffraction (XRD)

Figure 7 presents the XRD pattern of pristine WO_3NPs, POT, and POT/WO_3NPs nanocomposite *b*. Since there is no considerable change in results obtained from XRD patterns of nanocomposite *a* and *c*, we here just consider nanocomposite *b* [$(mol_{WO_3}/mol_{monomer})\cdot 100 = 65\%$].

Based on observed diffraction peaks in the XRD pattern of WO_3NPs, the polygonal formation can be indicated. The POT XRD pattern where the broad peak around 2θ = 20–30° shows the amorphous character of in-situ oxidative polymerized POT [114, 116].

The XRD pattern of POT/WO_3NPs *b* in Figure 7 proposes that the important diffraction peaks of WO_3NPs are also available in POT/WO_3NPs. This is good evidence that the crystallization efficiency of the WO_3NPs was not affected owing to the POT. It affirms that, based on our expectation, chemical transformation in the WO_3NPs does not occur upon mixing them with POT. It is also clear that the POT broad peak overlaps with the high diffraction intensities of (200), (020), and (002) crystal faces of WO_3NPs.

3.6. Elemental analysis (CHN)

Table 3 presents the results computed from the analysis of CHN. The POT/WO_3NPs *b* structure is illustrated in Figure 1 based on the FT-IR and CHN analyses.

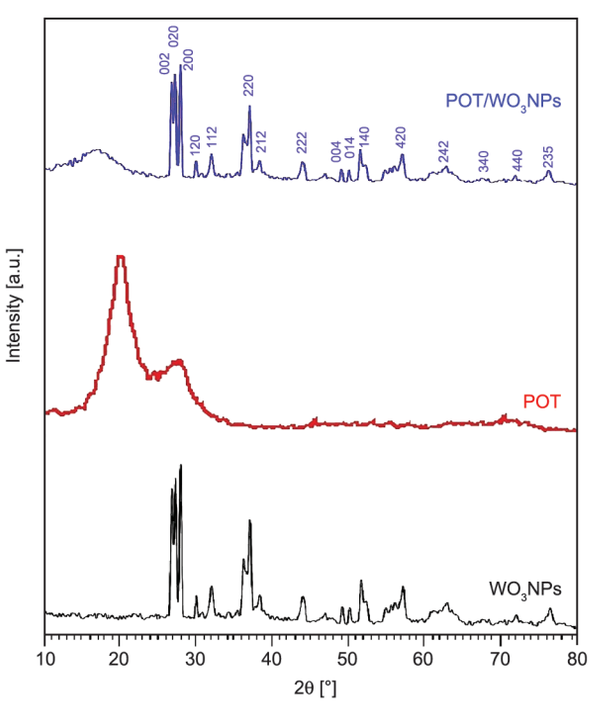

Figure 7. XRD patterns of WO_3NPs, POT, and POT/WO_3NPs *b*.

Table 3. Elements ratio consisted of POT/WO_3NPs *b*.

		C	H	N	C/H	C/N
Weight ratio	[wt%]	18.61	1.95	2.95	0.79	7.33
Amount of substance element	[mol]	1.54	1.93	0.21		
Molar ratio	[–]	7.29	9.14	1.00		

Based on Table 3, the total weight percent of C, H, and N elements is 23.51%, that related to the polymeric part (POT) of the nanocomposite. The remaining percentage, which is 76.49%, is related to WO_3NPs, $FeCl_x$ ($FeCl_2$ and $FeCl_3$) coordinated with both the polymer and WO_3, chemically and physically (hydroxyl groups on the WO_3NPs surface) adsorbed water, and free acids (HCl) [66, 117–119]. The results of CHN analysis are also supported using TGA analysis which is described in the following sections. Consequently, the proposed POT/WO_3NPs b formula was confirmed by elemental analysis data and TGA.

3.7. Thermal properties

As illustrated in Figure 8, the TGA was carried out in a flowing air atmosphere to realize the POT and nanocomposite's (POT/WO_3NPs *b*) decomposition process. POT showed two stages of weight loss: (i) weight (38%) loss in the range of 100–260 °C, can be attributed to the loss of physically adsorbed water molecules, HCl, and other volatile materials/solvent, (ii) weight (62%) loss up to 600 °C can be assigned to polymer degradation [84–87, 117–119]. The POT/WO_3NPs *b* showed the 11.9% weight loss in the temperature range from 40 to 254 °C, attributed to the removal of unreacted monomers, physically adsorbed water, and free acids (HCl). Furthermore, 27.8% of weight loss was observed when the temperature was between 254 to 541 °C. It can be attributed to the POT decomposition process, which is 23.51% from CHN results, and the removal of $FeCl_2$ and $FeCl_3$ coordinated with both the polymer and WO_3 and adsorbed chemical water (hydroxyl groups on the WO_3NPs surface) that these are about residue 4.3% [66, 117–119]. The 60% residual value in TGA analysis is related to WO_3NPs and iron oxides.

A comparison of the actual composition ratio of POT and WO_3NPs of nanocomposites with the amount of raw materials used in the synthesis confirms the coating of WO_3NPs by a thin layer of POT with core-shell morphology observed in TEM images (next section). Indeed, the excess value of POT was washed in work up.

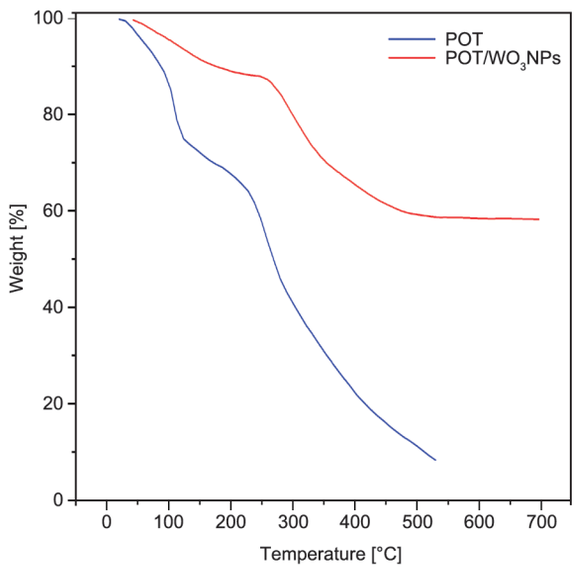

Figure 8. TGA curves of POT and POT/WO_3NPs *b* under an air atmosphere at 10 °C·min^{-1} heating rate.

3.8. Morphology analysis

The FE-SEM (Figure 9a–9c) and TEM (Figure 9d, 9e) were used to investigate the size, morphology, and dispersion ability of WO_3NPs, POT, and POT/WO_3NPs *b*. Since there is no considerable change in results obtained from FE-SEM and morphology analysis of nanocomposite *a* and *c*, we here just consider nanocomposite *b* [($mol_{WO_3}/mol_{monomer}$)·100 = 65%]. Figure 9a shows the FE-SEM micrograph of WO_3NPs made ready by precipitation technique. Accordingly, it can be stated that approximately polygonal-shaped WO_3NPs with sizes between 60–100 nm are uniformly distributed with porous morphology. It is obvious that the pure POT (Figure 9b) has a well-developed amorphous morphology with nearly similar diameters. From the TEM images of POT/WO_3NPs *b* (Figure 9d, 9e), it can be seen that the WO_3NPs are uniformly distributed and well implanted within the POT matrix. Based on our observation, it is clear that the nanocomposite particles had polygonal shapes. Furthermore, the core-shell morphology with a core of WO_3NPs (71.42 nm diameter) and shell of POT (5.84 nm diameter) was observed in TEM images (Figure 9d, 9e) because of dark and light areas. Figure 1 shows a schematic diagram of the nanocomposite core-shell structure formation.

3.9. Conductivity measurement

The compact tablets were employed for measuring the electrical conductivity of samples utilizing the DC 4-probe conventional technique at the *RT*. The POT, WO_3NPs, and POT/WO_3NPs *b* conductivities are respectively about $7.18\cdot10^{-2}$, 0.041, and 0.82 S·cm^{-1} at the *RT* (25 °C). According to the empirical results, it can be said that the electrical conductivity of WO_3NPs is remarkably enhanced by modifying the surface of WO_3NPs by the semiconductor POT.

The obtained results indicate that the most important charge carriers in the POT/WO_3NPs are embedded in the POT structure. Facilitating carrier transport between different POT molecular chains using WO_3NPs can be considered as another reason for enhancing electrical conductivity. As a matter of fact, an interaction at the junction P–N of POT and WO_3NPs is known as a potential reason for increasing the conjugation length in POT chains [120, 121]. These outcomes are in accordance with the results of UV-vis, which increases the electrical conductivity by reducing the POT/WO_3NPs band gap compared to the POT band gap (see 3.10 Section for a detailed discussion). A comparison of electrical conductivities of various samples based on POT and WO_3NPs is presented in Table 4.

3.10. Photovoltaic performance

Figure 10 displays the *J–V* specifications of the FTO|TiO_2NPs|POT|Al and FTO|TiO_2NPs|POT/WO_3NPs *a-c* |Al devices measured under AM 1.5 simulated solar rays at the *RT* (25 °C) while Table 5 summarizes the average values of the performance parameters of nanocomposites *a-c*. The results obtained of performance of solar cells fabricated from nanocomposites *a* and *c*, and the standard errors calculated.

The photovoltaic attributes that are mentioned here are only information on the efficient synthesis of hybrid solar cells with POT and WO_3NPs as P–N heterojunction bilayer, bulk heterojunction, and both of them. The different photovoltaic characteristics like fill factor (*FF*), the short circuit current (J_{SC}), power conversion efficiency (η or PCE), and open-circuit voltage (V_{OC}) were computed under these conditions. They were also regenerated several times without any important alternation. The fill factor was computed based on Equation (8) [122]:

$$FF = \frac{J_{max} \cdot V_{max}}{J_{SC} \cdot V_{OC}} \tag{8}$$

The energy conversion efficiency (η) was also measured using Equation (9) [123, 124]:

$$\eta = \frac{P_{out}}{P_{in}} = \frac{FF \cdot J_{max} \cdot V_{max}}{P_{in}} \quad (9)$$

Since the results obtained from the various analysis did not show a significant difference in the nanocomposites *a-c* considering the standard errors calculated,

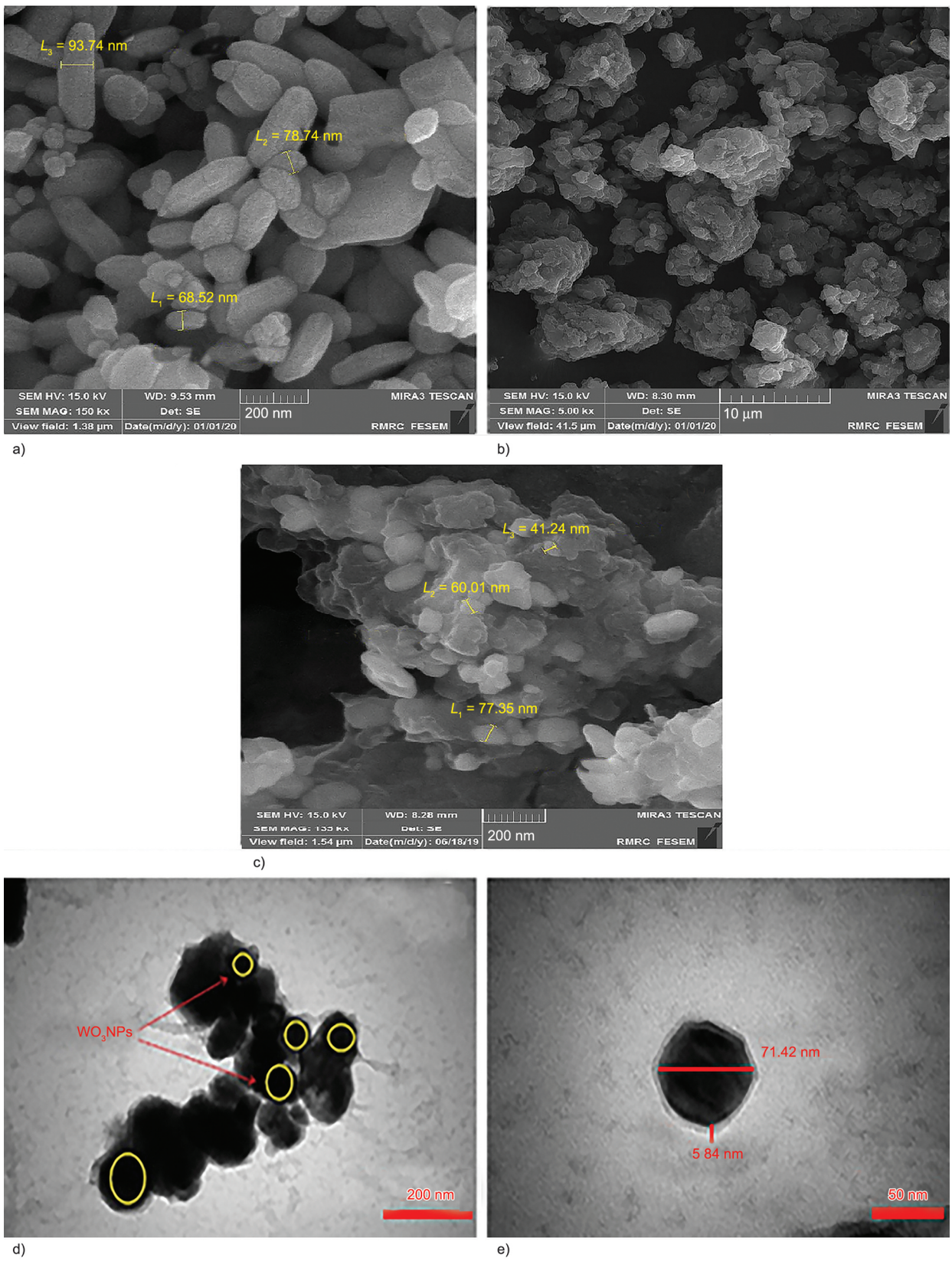

Figure 9. a) FE-SEM image of WO_3NPs, b) FE-SEM images of POT, c) FE-SEM images of POT/WO_3NPs *b*, and d), e) TEM images of POT/WO_3NPs *b*.

Table 4. Comparison of electrical conductivities of different samples based on POT and WO_3NPs.

Samples	Conductivity [S·cm^{-1}]	References
PAN/PANI/WO_3	0.110	[121]
POT	$1.49\cdot10^{-7}$	[33]
WO_3NPs	0.041	This work
POT	$7.18\cdot10^{-2}$	This work
POT/WO_3NPs *b*	0.82	This work

the average value of them was considered, as shown in nanocomposite *b*.

Under the illumination of a solar simulator, the performance of fabricated solar cells by POT and nanocomposites *a-c* was evaluated. The J_{SC}, V_{OC}, and *FF* values for FTO|TiO_2NPs|POT|Al solar cell were obtained at about 1.20 mA·cm^{-2}, 0.52 V, and 0.29%, respectively. Also the average value of J_{SC}, V_{OC}, and *FF* for the FTO|TiO_2NPs|POT/WO_3NPs *a-c*|Al solar cells were about 2.74 mA/cm^{-2}, 0.70 V, and 0.28%, respectively. Moreover, the power conversion efficiency (PCE) of solar cells fabricated by POT and POT/WO_3NPs *a-c* were 0.18 and 0.57%, respectively. As can be seen in Figure 10 and Table 5, a final optimized conversion performance for the POT/WO_3NPs tool was achieved at around 0.57%.

The motion of electrons and holes is shown in Figure 11. As observed, after exciton generation, electrons move from POT/WO_3NPs *b* to TiO_2NPs and then to FTO. Reversely, holes move from TiO_2NPs to POT/WO_3NPs *b* and then to Al.

The photovoltaic cell parameters and specifications (*FF*, J_{SC}, V_{OC}, and PCE) of the fabricated hybrid solar cells were also compared with previously reported data where only polyaniline, POT, and WO_3NPs are used as an active substance in a hybrid photovoltaic cell [48]. This comparison is shown in Table 6.

Having a stable organic component can be considered one of the prominent and efficient factors of hybrid inorganic-organic solar cells that should not be underrated. Generally, the focus of the chemical decomposition of the organic polymer part is largely on the reaction of water, oxygen, and electrode material with the active polymer layer. Apparently, although traces of oxygen are absorbed and penetrate in different layers along with the fabrication of the device, the diffusion into the finished device is assumed to be more significant [125]. Moreover, oxygen is easily activated using UV-vis illumination in the existence of sensitizers, such as organic molecules or tungsten trioxide. Any present organic substances (such as active and conducting polymers) can be aggressively attacked by the peroxide intermediates

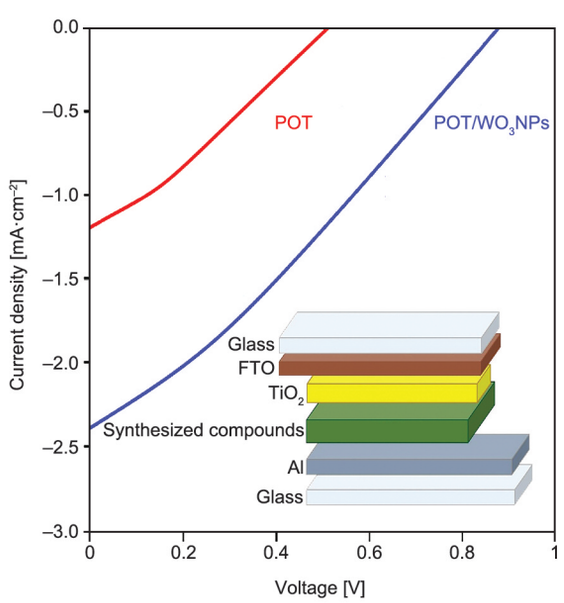

Figure 10. *J–V* curves of FTO|TiO_2NPs|POT|Al and FTO|TiO_2NPs|POT/WO_3NPs *b* | Al solar cells.

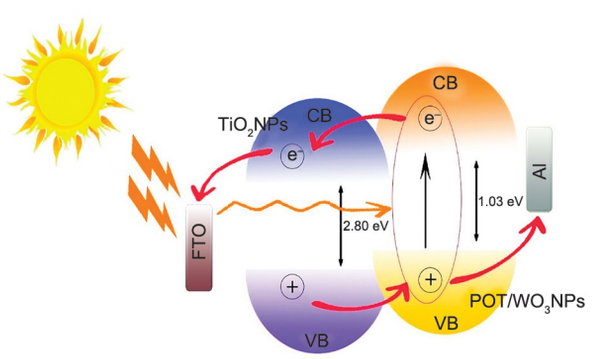

Figure 11. The motion of electrons and hole in FTO|TiO_2NPs|POT/WO_3NPs *b* | Al solar cell.

Table 5. Average values[b] of J_{SC}, V_{OC}, J_{max}, V_{max}, *FF*, and η of the fabricated photovoltaic cells from nanocomposites *a-c*.

Device	J_{SC} [mA·cm^{-2}]	V_{OC} [V]	J_{max} [mA·cm^{-2}]	V_{max} [V]	*FF* [–]	η[a] [%]
FTO| TiO_2NPs| POT| Al	1.20	0.52	0.74	0.25	0.29	0.18
FTO| TiO_2NPs| POT/WO_3NPs *a-c*| Al[b]	2.74	0.70	1.50	0.39	0.28	0.57

[a]η [%] = $P_{max}\cdot100/(P\cdot Sea)$, cell area = 1 cm^2.

[b]Since the results obtained from various analyses did not show a significant difference in the nanocomposites *a-c* considering the standard errors calculated, the average value of them was considered.

Table 6. Comparison of solar cell parameters and characteristics (J_{SC}, V_{OC}, *FF* and η) of this work with similar previous reports.

Entry	Device	Action of POT	J_{SC} [mA·cm^{-2}]	V_{OC} [V]	*FF* [–]	η [%]	References
1	Al/POT-nSi/Al	Hole transport layer	1.70	0.22	0.235	0.88	[33]
2	ITO/PANI-poly(BuA/VAc)/electrolyte/Pt	Active layer	0.022	0.140	0.22	0.115	[141]
3	ITO/HAPAN-HCl/P3HT:PC71BM/Al	Buffer layer	8.39	0.611	0.722	3.70	[142]
4	FTO/Sb2S3 (thick)TiO_2NPs/PANI/Pt	Hole transport layer	1.76	0.937	0.531	0.88	[143]
5	ITO/PTCDA-PANI/N719/electrolyte/Al	Hole transport layer	10.25	0.67	0.42	2.88	[144]
6	ITO/PANI-P3HT:PCBM/Al	Hole transport layer	8.97	0.55	0.49	2.48	[145]
7	FTO/TiO_2NPs/WO_3 (5%)/H_2PtCl_6 (37.5% Pt basis)	Electron transport layer	12.92	0.72	63.33	5.89	[146]
8	FTO/TiO_2NPs/WO_3 (10%)/H_2PtCl_6 (37.5% Pt basis)	Electron transport layer	13.36	0.70	57.44	5.38	[146]
9	FTO/TiO_2NPs/WO_3 (15%)/H_2PtCl_6 (37.5% Pt basis)	Electron transport layer	12.60	0.67	57.44	4.89	[146]
10	FTO/WO_3 spin-coated PAN/PANI nanofibers (PANI content = 10 wt %)	Hole transport layer	11.78	0.66	0.35	2.72	[120]
11	FTO/PAN/PANI/WO_3 blend nanofibers	Hole transport layer	7.92	0.62	0.35	1.71	[121]
12	FTO/TiO_2NP/WO_3/perovskite/ spiro-OMeTAD/Ag	Electron transport layer	23.42	1.06	72.41	17.96	[147]
13	FTO| TiO_2NPs| POT| Al	Hole transport layer	2.01	0.67	0.27	0.18	This work
14	FTO| TiO_2NPs| POT/WO_3NPs *a-c*| Al[a]	Hole transport layer	2.74	0.70	0.28	0.57	This work

[a]Since the results obtained from various analyses did not show a significant difference in the nanocomposites *a-c* considering the standard errors calculated, the average value of them was considered.

(and radicals obtained from them) which result in oxidative decomposition.

PANI and its derivatives have been identified as radical scavengers [56, 126]. PANI can thwart free radicals by donating electrons, thereby altering their oxidation state from emeraldine to pernigraniline. The photovoltaic outcomes reported in the literature show that the cells containing PANI have a much more stable performance [125–130].

The photovoltaic effect consists of four basic stages, including light absorption, electron-hole production, charge transfer, and its collection. Light absorption occurs when materials are semiconductors in nature that can respond to incoming light. Absorption properties depend on their intrinsic absorption coefficient. The next step is electron-hole production. When incoming light strikes ground-state electrons in mineral semiconductor compounds, the charge carriers produce electrons and free holes [131–135]. In organic semiconductors, however, the excited electrons slowly relax and produce excitons. Most excitons are formed at the interface between TiO_2NPs and POT/WO_3NPs. To build an efficient organic photovoltaic cell, proper separation of excitons is key because the exciton bond energy is very large [136, 137]. In the next step, an exciton is dissociated into a free charge carrier and then collected by the individual electrode. This step involves transferring the separated charges to the electrodes through the charge transfer paths. Electrons are transported to FTO via TiO_2NPs and holes to Al via POT/WO_3NPs *b*.

We believe that HOMO (highest level of VB) and LUMO (lowest level of CB) of starting materials (POT and WO_3NPs) overlap together via hydrogen bonds, as its results are shown in Figure 12, and the new HOMO (highest level of VB) and LUMO (lowest level of CB), and the less band gap with a p-n heterojunction is created in result of donor-acceptor complex formation (hydrogen bonds) between POT and WO_3NPS [138–140].

The experimental outcomes clearly suggested that the nanocomposite exhibits a p-type semiconductor, which can be correlated with a p–n heterojunction created at the interface between n-type WO_3 and p-type POT [131–135]. What is certain, WO_3 exhibits n-type conductivity by electrons; thus, electron flow takes mainly place from n-WO_3 to p-POT until the balance and creates a common Fermi level (EF) in the n and p zones.

Hence, the p-n heterojunction produced by the mutual interaction, as illustrated in Figure 12, is the logical mechanism based on n-type (WO_3NPs) abandoning electrons to combine with holes in POT (p-type). We believe that there is a good overlapping

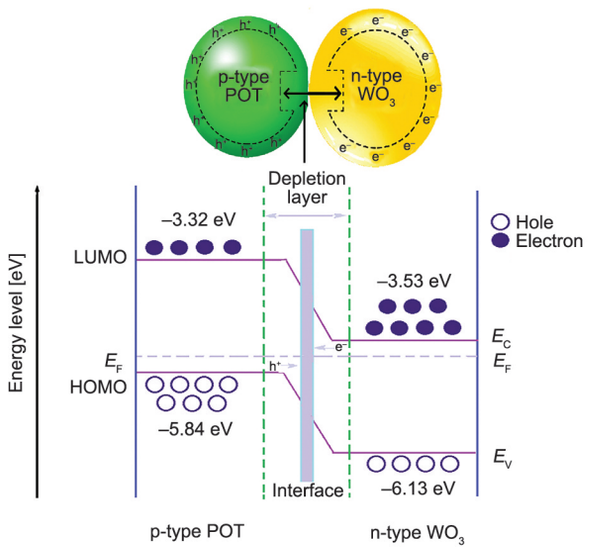

Figure 12. Schematic model for energy barrier at p-n junctions: The energy band structure diagram of p-type POT–n-type WO_3 heterojunction.

between HOMO (highest level of VB) and LUMO (lowest level of CB) of starting materials (POT and WO_3NPs) as above mentioned, and then, when the p-n heterojunction is in equilibrium, a narrow depletion area was formed at the hetero interface between POT and WO). As a result, the electron transfer between n-WO_3 and p-POT is less hampered, and thus, the energy barrier at p-n junctions is decreased, and conductivity is increased.

One of the outstanding aspects of our cell is that increasing WO_3NPs increases the efficiency of the cell about three times (entries 13 and 14 in Table 6). While Vu *et al*. [146] reported the efficiency of the DSSCs with the WO_3 nanoparticles was lower than those without WO_3. They explained these negative results by the higher recombination rate of holes and electrons and the smaller amount of dye absorbed on the PEs containing WO_3NPs. The results were negative because the conduction band (CB) of WO_3 is lower than that of TiO_2NPs. Therefore, the band structures in the WO_3/TiO_2NPs couple do not favor the separation of charge carriers. However, the conduction band (CB) of POT/WO_3NPs *b* (in this work) is higher than that of TiO_2NPs.

Reversely, You *et al*. [147]. reported positive results of increasing the WO_3 nanoparticles to perovskite solar cells by precisely controlling the thickness of the TiO_2NPs under layer. Their results are similar to our results.

4. Conclusions

To sum up, three POT/WO_3NPs nanocomposites *a-c* [$(mol_{WO_3}/mol_{monomer})\cdot 100$ = 60, 65, 70%] were effectively synthesized by an affordable and straightforward mechanochemical reaction in solid-state under the green condition and then their photovoltaic properties were investigated.

It is not observed that a considerable change in the IR (FT-IR), XRD, and morphology (FE-SEM) of the three nanocomposites *a-c*. Furthermore, their performance in the photovoltaic cells and standard errors calculated were evaluated. The results of photovoltaic properties show that nanocomposites do not have a significant difference in the efficiency of solar cells made of nanocomposites *a-c* considering the standard errors calculated.

TEM micrographs and XRD patterns of nanocomposite *b* reflected the presence of WO_3NPs polygonal and core-shell structures and also clarified that WO_3NPs were well incorporated in POT. This new nanocomposite demonstrated a red shift in the absorption edge, and a decrement in the optical band gap from 2.52 to 1.03 eV was observed [148, 149]. Moreover, the nanocomposite conductivity was 0.82 $S\cdot cm^{-1}$ at *RT* (25 °C).

The great photovoltaic device specifications obtained were on account of the particular morphology, structure, and the creation of heterojunction p-n bonds at the interfaces between POT and WO_3NPs. The outcomes indicated that the PSC is entirely efficient with a higher (η) compared to resembling cells in literature with less preparation costing, straightforward structure, and under an eco-friendly condition.

We believe that the POT/WO_3NPs nanocomposites can open inventive pathways for the development of other POT-based hybrid materials (nanocomposites) proper for preparing solar cells with the potential application value in an area of photovoltaic devices, which is a subject of the research study is ongoing.

Acknowledgements

The authors acknowledge the financial support of a grant from the Graduate Council of University of Sistan and Baluchestan and the National Nanotechnology Initiative funded by the Iranian government.

References

[1] Winter M., Brodd R. J.: What are batteries, fuel cells, and supercapacitors? Chemical Reviews, **104**, 4245–4270 (2004). https://doi.org/10.1021/cr020730k

[2] Lin N., Liu X.: Correlation between hierarchical structure of crystal networks and macroscopic performance of mesoscopic soft materials and engineering principles. Chemical Society Reviews, **44**, 7881–7915 (2015). https://doi.org/10.1039/C5CS00074B

[3] Yao W., Dai Q., Liu Y., Zhang Q., Zhong S., Yan Z.: Microwave-assisted synthesis of Co_3O_4 sheets for reversible Li storage: Regulation of structure and performance. ChemElectroChem, **4**, 1236–1242 (2017). https://doi.org/10.1002/celc.201700096

[4] Nie L., Zhang Q., Hu L., Liu Y., Yan Z.: Modified hydrazone derivatives for ratiometric and colorimetric F^- recognition: Relationship between architectures and performances. Sensors and Actuators B: Chemical, **245**, 314–320 (2017). https://doi.org/10.1016/j.snb.2017.01.152

[5] Yan Z., Hu L., Nie L., You J.: One-pot preparation of graphene–Ag nano composite for selective and environmentally-friendly recognition of trace mercury(II). RSC Advances, **6**, 109857–109861 (2016). https://doi.org/10.1039/C6RA16810H

[6] Sanchez C., Julián B., Belleville P., Popall M.: Applications of hybrid organic–inorganic nanocomposites. Journal of Materials Chemistry, **15**, 3559–3592 (2005). https://doi.org/10.1039/B509097K

[7] MacDiarmid A. G.: Polyaniline and polypyrrole: Where are we headed? Synthetic Metals, **84**, 27–34 (1997). https://doi.org/10.1002/chin.199729269

[8] MacDiarmid A. G.: 'Synthetic metals': A novel role for organic polymers (Nobel lecture). Angewandte Chemie, **40**, 2581–2590 (2001). https://doi.org/10.1002/1521-3773(20010716)40:14<2581::AID-ANIE2581>3.0.CO;2-2

[9] Hu L., Gruner G., Li D., Kaner R. B., Cech J.: Patternable transparent carbon nanotube films for electrochromic devices. Journal of Applied Physics, **101**, 016102 (2007). https://doi.org/10.1063/1.2402330

[10] Joseph N., Varghese J., Sebastian M. T.: Self assembled polyaniline nanofibers with enhanced electromagnetic shielding properties. RSC Advances, **5**, 20459–20466 (2015). https://doi.org/10.1039/C5RA02113H

[11] Joseph N., Varghese J., Sebastian M. T. A.: Facile formulation and excellent electromagnetic absorption of room temperature curable polyaniline nanofiber based inks. Journal of Materials Chemistry C, **4**, 999–1008 (2016). https://doi.org/10.1039/C5TC03080C

[12] Eftekhari A.: Nanostructured conductive polymers. Wiley, Cincinnati (2011).

[13] Stejskal J., Prokeš J.: Conductivity and morphology of polyaniline and polypyrrole prepared in the presence of organic dyes. Synthetic Metals, **264**, 116373 (2020). https://doi.org/10.1016/j.synthmet.2020.116373

[14] Ćirić-Marjanović G.: Recent advances in polyaniline research: Polymerization mechanisms, structural aspects, properties and applications. Synthetic Metals, **177**, 1–47 (2013). https://doi.org/10.1016/j.synthmet.2013.06.004

[15] Stejskal J.: Conducting polymers are not just conducting: A perspective for emerging technology. Polymer International, **69**, 662–664 (2019). https://doi.org/10.1002/pi.5947

[16] Mu S., Chen C., Wang J.: The kinetic behavior for the electrochemical polymerization of aniline in aqueous solution. Synthetic Metals, **88**, 249–254 (1997). https://doi.org/10.1016/S0379-6779(97)03863-0

[17] Baker C. O., Huang X., Nelson W., Kaner R. B.: Polyaniline nanofibers: Broadening applications for conducting polymers. Chemical Society Reviews, **46**, 1510–1525 (2017). https://doi.org/10.1039/C6CS00555A

[18] Trchová M., Stejskal J.: Polyaniline: The infrared spectroscopy of conducting polymer nanotubes (IUPAC technical report). Pure and Applied Chemistry, **83**, 1803–1817 (2011). https://doi.org/10.1351/PAC-REP-10-02-01

[19] Stejskal J.: Interaction of conducting polymers, polyaniline and polypyrrole, with organic dyes: Polymer morphology control, dye adsorption and photocatalytic decomposition. Chemical Papers, **74**, 1–54 (2020). https://doi.org/10.1007/s11696-019-00982-9

[20] Lan Z., Wu J., Gao S., Lin J., Huang M., Chen X.: Template-free synthesis of polyaniline nanobelts as a catalytic counter electrode in dye-sensitized solar cells. Polymers for Advanced Technologies, **25**, 343–346 (2014). https://doi.org/10.1002/pat.3246

[21] Kuo M., Cheng T-C., Ye H-K., Wang T-L., Wu T-H., Kuo C-C., Lee R-H.: Polyaniline/Ag_2S–CdS nanocomposites as efficient electrocatalysts for triiodide reduction in dye-sensitized solar cells. Catalysts, **11**, 507 (2021). https://doi.org/10.3390/catal11040507

[22] Tang Q., Cai H., Yuan S., Wang X.: Counter electrodes from double-layered polyaniline nanostructures for dye-sensitized solar cell applications. Journal of Materials Chemistry A, **1**, 317–323 (2013). https://doi.org/10.1039/C2TA00026A

[23] Hsu Y-C., Tseng L-C., Lee R-H.: Graphene oxide sheet–polyaniline nanohybrids for enhanced photovoltaic performance of dye-sensitized solar cells. Journal of Polymer Science Part B: Polymer Physics, **52**, 321–332 (2014). https://doi.org/10.1002/polb.23416

[24] Granot E., Basnar B., Cheglakov Z., Katz E., Willner I.: Enhanced bioelectrocatalysis using single-walled carbon nanotubes (SWCNTs)/polyaniline hybrid systems in thin-film and microrod structures associated with electrodes. Electroanalysis, **18**, 26–34 (2006). https://doi.org/10.1002/elan.200503403

[25] Granot E., Katz E., Basnar B., Willner I.: Enhanced bioelectrocatalysis using Au-nanoparticle/polyaniline hybrid systems in thin films and microstructured rods assembled on electrodes. Chemistry of Materials, **17**, 4600–4609 (2005). https://doi.org/10.1021/cm050193v

[26] Li D., Huang J., Kaner R. B.: Polyaniline nanofibers: A unique polymer nanostructure for versatile applications. Accounts of Chemical Research, **42**, 135–145 (2009). https://doi.org/10.1021/ar800080n

[27] Trchová M., Šeděnková I., Konyushenko E. N., Stejskal J., Holler P., Ćirić-Marjanović G.: Evolution of polyaniline nanotubes: The oxidation of aniline in water. The Journal of Physical Chemistry B, **19**, 9461–9468 (2006). https://doi.org/10.1021/jp057528g

[28] Huang J., Kaner R. B.: Nanofiber formation in the chemical polymerization of aniline: A mechanistic study. Angewandte Chemie, **43**, 5817–5821 (2004). https://doi.org/10.1002/anie.200460616

[29] Abd Razak S. I., Wahab I. F., Fadil F., Dahli F. N., Md Khudzari A. Z., Adeli H.: A review of electrospun conductive polyaniline based nanofiber composites and blends: Processing features, applications, and future directions. Advances in Materials Science and Engineering, **2015**, 356286 (2015). https://doi.org/10.1155/2015/356286

[30] Lan Z., Zhang X., Wu J., Lin J., Huang M., Zhao H.: A novel photoelectrochemical solar cell with high efficiency in converting ultraviolet light to electricity. Electrochimica Acta, **108**, 337–342 (2013). https://doi.org/10.1016/j.electacta.2013.06.121

[31] Wan M., Yang J.: Studies on the structure and electrical properties of poly(ortho-toluidine). Synthetic Metals, **73**, 201–204 (1995). https://doi.org/10.1016/0379-6779(95)80016-6

[32] Bavastrello V., Carrara S., Ram M. K., Nicolini C.: Optical and electrochemical properties of poly(*o*-toluidine) multiwalled carbon nanotubes composite Langmuir–Schaefer films. Langmuir, **20**, 969–973 (2004). https://doi.org/10.1021/la035372a

[33] Ziadan K. M., Hussein H. F., Ajeel K. I.: Study of the electrical characteristics of poly(*o*-toluidine) and application in solar cell. Energy Procedia, **18**, 157–164 (2012). https://doi.org/10.1016/j.egypro.2012.05.027

[34] Ruxangul J., Tursun A., Nurulla I.: Comparative studies of solid-state synthesized poly(*o*-methoxyaniline) and poly (*o*-toluidine). Polymers for Advanced Technologies, **19**, 1461–1466 (2008). https://doi.org/10.1002/pat.1139

[35] MacDiarmid A. G., Chiang J-C., Hapern M., Huang W-S., Mu L., Nanaxakkara L. D., Samasiri N. L. C., Wu S. W., Yaniger S. I.: Polyaniline: Interconversion of metallic and insulating forms. Molecular Crystals and Liquid Crystals, **121**, 173–180 (1985). https://doi.org/10.1080/00268948508074857

[36] Focke W. W., Wnek G. E., Wei Y. J.: Influence of oxidation state, pH, and counterion on the conductivity of polyaniline. The Journal of Physical Chemistry, **91**, 5813–5818 (1987). https://doi.org/10.1021/J100306A059

[37] Pron A., Genoud F., Menardo C., Nechtschein M.: The effect of the oxidation conditions on the chemical polymerization of polyaniline. Synthetic Metals, **24**, 193–201 (1988). https://doi.org/10.1016/0379-6779(88)90257-3

[38] Yasuda A., Shimidzu T.: Chemical oxidative polymerization of aniline with ferric chloride. Polymer Journal, **25**, 329–338 (1993). https://doi.org/10.1295/polymj.25.329

[39] Ding H., Liu X-M., Wan M., Fu S-Y.: Electromagnetic functionalized cage-like polyaniline composite nanostructures. The Journal of Physical Chemistry B, **112**, 9289–9294 (2008). https://doi.org/10.1021/jp8016997

[40] Genies E. M., Syed A. A., Tsintavis C.: Electrochemical study of polyaniline in aqueous and organic medium. Redox and kinetic properties. Molecular Crystals and Liquid Crystals, **121**, 181–186 (1985). https://doi.org/10.1080/00268948508074858

[41] Wei H., Yan X., Wu S., Luo Z., Wei S., Guo Z.: Electropolymerized polyaniline stabilized tungsten oxide nanocomposite films: Electrochromic behavior and electrochemical energy storage. The Journal of Physical Chemistry C, **116**, 25052–25064 (2012). https://doi.org/10.1021/jp3090777

[42] Lee S-H., Deshpande R., Parilla P. A., Jones K. M., To B., Mahan A. H., Dillon A. C.: Crystalline WO) nanoparticles for highly improved electrochromic applications. Advanced Materials, **18**, 763–766 (2006). https://doi.org/10.1002/adma.200501953

[43] Zhang J., Wang X. L., Xia X. H., Gu C. D., Zhao Z. J., Tu J. P.: Enhanced electrochromic performance of macroporous WO_3 films formed by anodic oxidation of DC-sputtered tungsten layers. Electrochimica Acta, **55**, 6953–6958 (2010). https://doi.org/10.1016/j.electacta.2010.06.082

[44] Wang J., Khoo E., Lee P. S., Ma J.: Synthesis, assembly, and electrochromic properties of uniform crystalline WO_3 nanorods. The Journal of Physical Chemistry C, **112**, 14306–14312 (2008). https://doi.org/10.1021/jp804035r

[45] Granqvist C.: Electrochromic tungsten oxide films: Review of progress 1993–1998. Solar Energy Materials and Solar Cells, **60**, 201–262 (2000). https://doi.org/10.1016/S0927-0248(99)00088-4

[46] Sadek A. Z., Wlodarski W., Shin K., Kaner R. B., Kalantar-zadeh K.: A polyaniline/WO_3 nanofiber composite-based ZnO/64° YX $LiNbO_3$ SAW hydrogen gas sensor. Synthetic Metals, **158**, 29–32 (2008). https://doi.org/10.1016/j.synthmet.2007.11.008

[47] Najafi-Ashtiani H., Bahari A.: Optical, structural and electrochromic behavior studies on nanocomposite thin film of aniline, *o*-toluidine and WO_3. Optical Materials, **58**, 210–218 (2016). https://doi.org/10.1016/j.optmat.2016.05.035

[48] Janáky C., de Tacconi N. R., Chanmanee W., Rajeshwar K.: Electrodeposited polyaniline in a nanoporous WO_3 matrix: An organic/inorganic hybrid exhibiting both p- and n-type photoelectrochemical activity. The Journal of Physical Chemistry C, **116**, 4234–4242 (2012). https://doi.org/10.1021/jp211698j

[49] Wei H., Yan X., Wu S., Luo Z., Wei S., Guo Z.: Electropolymerized polyaniline stabilized tungsten oxide nanocomposite films: Electrochromic behavior and electrochemical energy storage. The Journal of Physical Chemistry C, **116**, 25052–25064 (2012). https://doi.org/10.1021/jp3090777

[50] Kumar R., Yadav B. C.: Fabrication of polyaniline (PANI)-tungsten oxide (WO_3) composite for humidity sensing application. Journal of Inorganic and Organometallic Polymers and Materials, **26**, 1421–1427 (2016). https://doi.org/10.1007/s10904-016-0412-9

[51] Lin X., Jiang C.: Self-assembly of molybdophosphate on a glassy carbon electrode covalently modified with choline and electrocatalytic reduction of iodate. Analytical Sciences, **22**, 697–700 (2006). https://doi.org/10.2116/analsci.22.697

[52] Huang X., Li Y., Chen Y., Wang L.: Electrochemical determination of nitrite and iodate by use of gold nanoparticles/poly(3-methylthiophene) composites coated glassy carbon electrode. Sensor and Actuators B: Chemical, **134**, 780–786 (2008). https://doi.org/10.1016/j.snb.2008.06.028

[53] Ponzio E. A., Benedetti T. M., Torresi R. M.: Electrochemical and morphological stabilization of V_2O_5 nanofibers by the addition of polyaniline. Electrochimica Acta, **52**, 4419–4427 (2007). https://doi.org/10.1016/j.electacta.2006.12.023

[54] Kong L., Lu X., Zhang W.: Facile synthesis of multifunctional multiwalled carbon nanotubes/Fe_3O_4 nanoparticles/polyaniline composite nanotubes. Journal of Solid State Chemistry, **181**, 628–636 (2008). https://doi.org/10.1016/j.jssc.2008.01.006

[55] Sun L-J., Liu X-X., Lau K. K-T., Chen L., Gu W-M.: Electrodeposited hybrid films of polyaniline and manganese oxide in nanofibrous structures for electrochemical supercapacitor. Electrochimica Acta, **53**, 3036–3042 (2008). https://doi.org/10.1016/j.electacta.2007.11.034

[56] Yarmohamadi-Vasel M., Modarresi-Alam A. R., Noroozifar M., Hadavi M. S.: An investigation into the photovoltaic activity of a new nanocomposite of (polyaniline nanofibers)/(titanium dioxide nanoparticles) with different architectures. Synthetic Metals, **252**, 50–61 (2019). https://doi.org/10.1016/j.synthmet.2019.04.007

[57] Su P., Liu Y., Zhang J., Chen C., Yang B., Zhang C., Zhao X.: Pb-based perovskite solar cells and the underlying pollution behind clean energy: Dynamic leaching of toxic substances from discarded perovskite solar cells. The Journal of Physical Chemistry Letters, **11**, 2812–2817 (2020). https://doi.org/10.1021/acs.jpclett.0c00503

[58] Afzaal M., Yates H. M., Walter A., Nicolay S.: Improved FTO/NiO_x interfaces for inverted planar triple-cation perovskite solar cells. IEEE Journal of Photovoltaics, **9**, 1302–1308 (2019). https://doi.org/10.1109/JPHOTOV.2019.2927927

[59] Raj C. J., Rajesh M., Manikandan R., Sim J. Y., Yu K. H., Park S. Y., Song J. H., Kim B. C.: Two-dimensional planar supercapacitor based on zinc oxide/manganese oxide core/shell nan*o*-architecture. Electrochimica Acta, **247**, 949–957 (2017). https://doi.org/10.1016/j.electacta.2017.07.009

[60] Choi K., Lee J., Kim H. I., Park C. W., Kim G-W., Choi H., Park S., Park S. A., Park T.: Thermally stable, planar hybrid perovskite solar cells with high efficiency. Energy and Environmental Science, **11**, 3238–3247 (2018). https://doi.org/10.1039/C8EE02242A

[61] Supothina S., Seeharaj P., Yoriya S., Sriyudthsak M.: Synthesis of tungsten oxide nanoparticles by acid precipitation method. Ceramics International, **33**, 931–936 (2007). https://doi.org/10.1016/j.ceramint.2006.02.007

[62] Martínez-de la Cruz A., Sánchez Martínez D., López Cuellar E.: Synthesis and characterization of WO_3 nanoparticles prepared by the precipitation method: Evaluation of photocatalytic activity under vis-irradiation. Solid-State Chemistry, **12**, 88–94 (2010). https://doi.org/10.1016/j.solidstatesciences.2009.10.010

[63] Bonnot K., Grandcolas M., Keller V., Spitzer D.: Solid state and template free synthesis of a nanotubular polyaniline-TiO_2 composite. Nano Science and Technology Institute, **2**, 491–494 (2009).

[64] Du X-S., Zhou C-F., Wang G-T., Mai Y-W.: Novel solid-state and template-free synthesis of branched polyaniline nanofibers. Chemistry of Materials, **20**, 3806–3808 (2008). https://doi.org/10.1021/cm800689b

[65] Zhou C-F., Du X-S., Liu Z., Ringer S. P., Mai Y-W.: Solid phase mechanochemical synthesis of polyaniline branched nanofibers. Synthetic Metals, **159**, 1302–1307 (2009). https://doi.org/10.1016/j.synthmet.2009.02.033

[66] Shabzendedar S., Modarresi-Alam A. R., Noroozifar M., Mansouri-Torshizi H.: Synthesis and characterization of poly(p-aminoazobenzene) nanosheet as a new derivative of polyaniline containing azo groups under green chemistry condition and its high efficiency in solar cell. Synthetic Metals, **255**, 116115 (2019). https://doi.org/10.1016/j.synthmet.2019.116115

[67] Padinger F., Brabec C. J., Fromherz T., Hummelen J. C., Sariciftci N. S.: Fabrication of large area photovoltaic devices containing various blends of polymer and fullerene derivatives by using the doctor blade technique. OptoElectronics, **8**, 280–283 (2000).

[68] Khamwannah J., Noh S. Y., Frandsen C., Zhang Y., Kim H., Kong S. D., Jin S.: Nanocomposites of TiO_2 and double-walled carbon nanotubes for improved dye-sensitized solar cells. Journal of Renewable and Sustainable Energy, **4**, 023116 (2012). https://doi.org/10.1063/1.4705117

[69] Badilescu S., Ashrit P. V.: Study of sol–gel prepared nanostructured WO_3 thin films and composites for electrochromic applications. Solid State Ionics, **158**, 187–197 (2003). https://doi.org/10.1016/S0167-2738(02)00764-6

[70] Sharbatdaran M., Novinrooz A., Noorkojouri H.: Preparation and characterization of WO_3 electrochromic films obtained by the sol-gel process. Iranian Journal of Chemistry and Chemical Engineering, **25**, 25–29 (2006). https://doi.org/10.30492/ijcce.2006.8076

[71] Geng L., Zhao Y., Huang X., Wang S., Zhang S., Wu S.: Characterization and gas sensitivity study of polyaniline/SnO_2 hybrid material prepared by hydrothermal route. Sensors and Actuators B: Chemical, **120**, 568–572 (2007). https://doi.org/10.1016/j.snb.2006.03.009

[72] Husain J., Chacradhar S. B., Prasad M. V. N. A.: Studies on electrical and sensing properties of polyaniline/iron oxide (α-Fe_2O_3) nanocomposites. International Journal of Research in Industrial Engineering, **4**, 198–202 (2014).

[73] McNally T., Olenik I. D.: Composites of inorganic nanotubes and polymers. Physica Status Solidi A, **210**, 2249–2251 (2013). https://doi.org/10.1002/pssa.201370073

[74] Ziadan K. M., Hussein H. F., Ajeel K. I.: Study of the electrical characteristics of poly(*o*-toluidine) and application in solar cell. Energy Procedia, **18**, 157–164 (2012). https://doi.org/10.1016/j.egypro.2012.05.027

[75] Khuspe G. D., Navale S. T., Bandgar D. K., Sakhare R. D., Chougule M. A., Patil V. B.: SnO_2nanoparticles-modified polyaniline films as highly selective, sensitive, reproducible and stable ammonia sensors. Electronic Materials Letters, **10**, 191–197 (2014). https://doi.org/10.1007/s13391-013-3096-0

[76] Karami H., Asadi M. G., Mansoori M.: Pulse electropolymerization and the characterization of polyaniline nanofibers. Electrochimica Acta, **61**, 154–164 (2012). https://doi.org/10.1016/j.electacta.2011.11.097

[77] Kumar A., Ali V., Kumar S., Husain M.: Studies on conductivity and optical properties of poly(*o*-toluidine)-ferrous sulfate composites. International Journal of Polymer Analysis and Characterization, **16**, 298–306 (2011). https://doi.org/10.1080/1023666X.2011.587945

[78] Kulkarni M. V., Viswanath A. K., Mulik U. P.: Studies on chemically synthesized organic acid doped poly(*o*-toluidine). Materials Chemistry and Physics, **89**, 1–5 (2005). https://doi.org/10.1016/j.matchemphys.2004.01.031

[79] Hariharan V., Aroulmoji V., Sekar C., Shanthakumar A., Kumara Dhas M., Komagan E., Kalamegam K.: Synthesis of tungsten oxide (WO_3) nanoparticles with EDTA by microwave irradiation method. International Journal of Advanced Science and Engineering, **3**, 299–307 (2016).

[80] MacDiarmid A., Epstein A. J.: The concept of secondary doping as applied to polyaniline. Synthetic Metals, **65**, 103–116 (1994). https://doi.org/10.1016/0379-6779(94)90171-6

[81] Bian C., Yu Y., Xue G.: Synthesis of conducting polyaniline/TiO_2 composite nanofibres by one-step *in situ* polymerization method. Journal of Applied Polymer Science, **104**, 21–26 (2007). https://doi.org/10.1002/app.25636

[82] Izumi C. M., Constantino V. R. L., Ferreira A. M. C., Temperini M. L. A.: Spectroscopic characterization of polyaniline doped with transition metal salts. Synthetic Metals, **156**, 654–663 (2006). https://doi.org/10.1016/j.synthmet.2005.12.023

[83] Qiu B., Li Z., Wang X., Li X., Zhang J.: Exploration on the microwave-assisted synthesis and formation mechanism of polyaniline nanostructures synthesized in different hydrochloric acid concentrations. Journal of Polymer Science, **55**, 3357–3369 (2017). https://doi.org/10.1002/pola.28707

[84] Modarresi–Alam A. R., Farrokhzadeh A., Shabzendedar S., Sedighi–Darijani N.: Synthesis of daisy-shaped core–shell nanocomposites of chiral poly[(±)-2-(sec-butyl) aniline] in the solid state. Iranian Polymer Journal, **28**, 75–86 (2019). https://doi.org/10.1007/s13726-018-0679-5

[85] Zamani N., Modarresi–Alam A. R., Noroozifar M., Javanbakht M.: The improved performance of lithium-ion batteries *via* the novel electron transport catalytic role of polyaniline (PANI) in PANI/Co_3O_4–CuO raspberry as new anode material. Journal of Applied Electrochemistry, **49**, 327–340 (2019). https://doi.org/10.1007/s10800-019-01286-2

[86] Modarresi–Alam A. R., Soleimani M., Pakseresht M., Farzaneh–Jobaneh E., Zeraatkar V., Tabatabaei F. A., Shabzendedar S., Movahedifar F.: Preparation of new conductive nanocomposites of polyaniline and silica under solid-state condition (in Persian). Iranian Journal of Polymer Science and Technology, **29**, 387–398 (2016).
https://doi.org/10.22063/jipst.2016.1412

[87] Modarresi-Alam A. R., Zafari S., Miandashti A. R.: A facile preparation method for synthesis of silica sulfuric acid/poly(*o*-methoxyaniline) core–shell nanocomposite. Polymers for Advanced Technologies, **26**, 645–657 (2015).
https://doi.org/10.1002/pat.3499

[88] Sedighi-Darijani N., Modarresi-Alam A. R., Noroozifar M., Hadavi M. S.: Single-layer solar cell based on nanostructure of polyaniline on fluorine-doped tin oxide: A simple, low-cost and efficient FTO|n-PANI|Al cell. Journal of the Iranian Chemical Society, **15**, 967–980 (2018).
https://doi.org/10.1007/s13738-018-1294-2

[89] Zahn D. R., Gavrila G. N., Gorgoi M.: The transport gap of organic semiconductors studied using the combination of direct and inverse photoemission. Chemical Physics, **325**, 99–112 (2006).
https://doi.org/10.1016/j.chemphys.2006.02.003

[90] Djurovich P. I., Mayo E. I., Forrest S. R., Thompson M. E.: Measurement of the lowest unoccupied molecular orbital energies of molecular organic semiconductors. Organic Electronics, **10**, 515–520 (2009).
https://doi.org/10.1016/j.orgel.2008.12.011

[91] Ahmida M. M., Eichhorn S. H.: Measurements and prediction of electronic properties of discotic liquid crystalline triphenylenes and phthalocyanines. ECS Transactions, **25**, 1–10 (2010).
https://doi.org/10.1149/1.3314449

[92] Leonat L., Sbârcea G., Branîzoi I. V.: Cyclic voltammetry for energy levels estimation of organic materials. UPB Scientific Bulletin, Series B: Chemistry and Materials Science, **75**, 111–118 (2013).

[93] Zanatta A. R.: Revisiting the optical band gap of semiconductors and the proposal of a unified methodology to its determination. Scientific Reports, **9**, 11225 (2019).
https://doi.org/10.1038/s41598-019-47670-y

[94] Makuła P., Pacia M., Macyk W.: How to correctly determine the band gap energy of modified semiconductor photocatalysts based on UV-Vis spectra. The Journal of Physical Chemistry Letters, **9**, 6814–6817 (2018).
https://doi.org/10.1021/acs.jpclett.8b02892

[95] Escobedo Morales A., Sanchez Mora E., Pal U.: Use of diffuse reflectance spectroscopy for optical characterization of un-supported nanostructures. Revista Mexicana de Fisica, **53**, 18–22 (2007).

[96] Karkare M. M.: The direct transition and not indirect transition is more favourable for band gap calculation of anatase TiO_2 nano particles. International Journal of Scientific and Engineering Research, **6**, 48–53 (2015).

[97] Wang T., Daiber B., Frost J. M., Mann S. A., Garnett E. C., Walsh A., Ehrler B.: Indirect to direct band gap transition in methylammonium lead halide perovskite. Energy and Environmental Science, **10**, 509–515 (2017).
https://doi.org/10.1039/C6EE03474H

[98] Mojtabavi E. A., Nasirian S.: A self-powered UV photodetector based on polyaniline/titania nanocomposite with long-term stability. Optical Materials, **94**, 28–34 (2019).
https://doi.org/10.1016/j.optmat.2019.05.026

[99] Farag A. A. M., Ashery A., Shenashen M. A.: Optical absorption and spectrophotometric studies on the optical constants and dielectric of poly (*o*-toluidine) (POT) films grown by spin coating deposition. Physica B: Condensed Matter, **407**, 2404–2411 (2012).
https://doi.org/10.1016/j.physb.2012.03.034

[100] Ling M., Blackman C. S., Palgrave R. G., Sotelo-Vazquez C., Kafizas A., Parkin I. P.: Correlation of optical properties, electronic structure, and photocatalytic activity in nanostructured tungsten oxide. Advanced Materials Interfaces, **4**, 1700064 (2017).
https://doi.org/10.1002/admi.201700064

[101] Charles C., Martin N., Devel M., Ollitrault J., Billard A.: Correlation between structural and optical properties of WO_3 thin films sputter deposited by glancing angle deposition. Thin Solid Films, **534**, 275–281 (2013).
https://doi.org/10.1016/j.tsf.2013.03.004

[102] Ross-Medgaarden E. I., Wachs I. E.: Structural determination of bulk and surface tungsten oxides with UV-vis diffuse reflectance spectroscopy and Raman spectroscopy. The Journal of Physical Chemistry C, **111**, 15089–15099 (2007).
https://doi.org/10.1021/jp074219c

[103] Najafi-Ashtiani H., Bahari A.: Optical and cyclic voltammetry behavior studies on nanocomposite film of copolymer and WO_3 grown by electropolymerization. Synthetic Metals, **217**, 19–28 (2016).
https://doi.org/10.1016/j.synthmet.2016.03.008

[104] Miu E. V., McKone J. R.: Comparisons of WO_3 reduction to H_xWO_3 under thermochemical and electrochemical control. Journal of Materials Chemistry A, **7**, 23756–23761 (2019).
https://doi.org/10.1039/C9TA06394C

[105] Chang C-H., Huang T-K., Lin Y-T., Lin Y-Y., Chen C-W., Chu T-H., Su W-F.: Improved charge separation and transport efficiency in poly(3-hexylthiophene)–TiO_2nanorod bulk heterojunction solar cells. Journal of Materials Chemistry, **18**, 2201–2207 (2008).
https://doi.org/10.1039/B800071A

[106] Gusiak N., Kobasa I., Kurek S.: Organic dye sensitisers for solar cells and semiconductor photocatalysts-a method for suitability evaluation explained. Czasopismo Techniczne Chemia, **108**, 59–73 (2011).

[107] Hwang S-W., Chen Y.: Synthesis and electrochemical and optical properties of novel poly(aryl ether)s with isolated carbazole and p-quaterphenyl chromophores. Macromolecules, **34**, 2981–2986 (2001).
https://doi.org/10.1021/ma001855z

[108] Olgun U., Gülfen M.: Effects of different dopants on the band gap and electrical conductivity of the poly (phenylene-thiazolo[5,4-d]thiazole) copolymer. RSC Advances, **4**, 25165–25171 (2014). https://doi.org/10.1039/C4RA02425G

[109] Sathiyan G., Thangamuthu R., Sakthivel P.: Synthesis of carbazole-based copolymers containing carbazole-thiazolo[5,4-d]thiazole groups with different dopants and their fluorescence and electrical conductivity applications. RSC Advances, **6**, 69196–69205 (2016). https://doi.org/10.1039/C6RA08888K

[110] Kumar D.: Electrochemical and optical behaviour of conducting polymer: Poly(*o*-toluidine). European Polymer Journal, **35**, 1919–1923 (1999). https://doi.org/10.1016/S0014-3057(98)00178-5

[111] Hidalgo D., Bocchini S., Fontana M., Saracco G., Hernández S.: Green and low-cost synthesis of PANI–TiO_2 nanocomposite mesoporous films for photoelectrochemical water splitting. RSC Advances, **5**, 49429–49438 (2015). https://doi.org/10.1039/C5RA06734K

[112] Bhadra S., Khastgir D., Singha N. K., Lee J. H.: Progress in preparation, processing and applications of polyaniline. Progress in Polymer Science, **34**, 783–810 (2009). https://doi.org/10.1016/j.progpolymsci.2009.04.003

[113] Eftekhari A.: Nanostructured conductive polymers. Wiley, Cincinnati (2011).

[114] Wallace G. G., Teasdale P. R., Spinks G. M., Kane-Maguire L. A.: Conductive electroactive polymers: Intelligent materials systems. CRC Press, Boca Raton (2002). https://doi.org/10.1201/9781420031898

[115] Khuspe G. D., Bandgar D. K., Sen S., Patil V. B.: Fussy nanofibrous network of polyaniline (PANi) for NH_3 detection. Synthetic Metals, **162**, 1822–1827 (2012). https://doi.org/10.1016/j.synthmet.2012.08.022

[116] Gu H., Huang Y., Zhang X., Wang Q., Zhu J., Shao L., Haldolaarachchige N., Young D. P., Wei S., Guo Z.: Magnetoresistive polyaniline-magnetite nanocomposites with negative dielectrical propertiess. Polymer, **53**, 801–809 (2012). https://doi.org/10.1016/j.polymer.2011.12.033

[117] Sadegh F., Modarresi-Alam A. R., Noroozifar M., Mansouri-Torshizi H.: Solid-state synthesis of PANI-TiO_2 nanocomposite: Investigation of reaction conditions, nature of oxidant and electrical properties. Express Polymer Letters, **15**, 2–15 (2021). https://doi.org/10.3144/expresspolymlett.2021.2

[118] Shabzendedar S., Modarresi-Alam A. R., Bahrpeyma A., Noroozifar M., Kerman K.: Novel conductive multi-walled polymeric nanotubes of poly(diazoaminobenzene) for single-layer polymer solar cell. Reactive and Functional Polymers, **149**, 104529 (2020). https://doi.org/10.1016/j.reactfunctpolym.2020.104529

[119] Sadegh F., Modarresi-Alam A. R., Noroozifar M., Kerman K.: A facile and green synthesis of superparamagnetic Fe_3O_4@PANI nanocomposite with a core–shell structure to increase of triplet state population and efficiency of the solar cells. Journal of Environmental Chemical Engineering, **9**, 104942 (2021). https://doi.org/10.1016/j.jece.2020.104942

[120] Zhu J., Wei S., Zhang L., Mao Y., Ryu J., Mavinakuli P., Karki A. B., Young D. P., Guo Z.: Conductive polypyrrole/tungsten oxide metacomposites with negative permittivity. The Journal of Physical Chemistry C, **114**, 16335–16342 (2010). https://doi.org/10.1021/jp1062463

[121] Eslah S., Nouri M.: Synthesis and characterization of tungsten trioxide/polyaniline/polyacrylonitrile composite nanofibers for application as a counter electrode of DSSCs. Russian Journal of Electrochemistry, **55**, 291–304 (2019). https://doi.org/10.1134/S1023193519030054

[122] Salmi T., Bouzguenda M., Gastli A., Masmoudi A.: Matlab/Simulink based modeling of photovoltaic cell. International Journal of Renewable Energy Resources, **2**, 213–218 (2012).

[123] Kwong C. Y., Djurišić A. B., Chui P. C., Cheng K. W., Chan W. K.: Influence of solvent on film morphology and device performance of poly(3-hexylthiophene):TiO_2 nanocomposite solar cells. Chemical Physics Letters, **384**, 372–375 (2004). https://doi.org/10.1016/j.cplett.2003.12.045

[124] Seifi M., Soh A. B. C., Wahab N., Hassan M. K. B.: A comparative study of PV models in Matlab/Simulink. International Journal of Electrical and Computer Engineering, **7**, 122–127 (2013).

[125] Jørgensen M., Norrman K., Krebs F. C.: Stability/degradation of polymer solar cells. Solar Energy Materials and Solar Cells, **92**, 686–714 (2008). https://doi.org/10.1016/j.solmat.2008.01.005

[126] Mandanipour V., Noroozifar M., Modarresi-Alam A. R.: Preparation of modified sulfonated poly(styrene divinylbenzene) with polyaniline as a new polymer electrolyte membrane for direct methanol fuel cell. International Journal of Electrochemical Science, **11**, 5302–5317 (2016). https://doi.org/10.20964/2016.06.32

[127] Abdulrazzaq O., Bourdo S. E., Woo M., Saini V., Berry B. C., Ghosh A., Biris A. S.: Comparative aging study of organic solar cells utilizing polyaniline and PEDOT:PSS as hole transport layers. ACS Applied Materials and Interfaces, **7**, 27667–2767 (2015). https://doi.org/10.1021/acsami.5b08000

[128] Ecker B., Nolasco J. C., Pallares J., Marsal L. F., Posdorfer J., Parisi J., von Hauff E.: Degradation effects related to the hole transport layer in organic solar cells. Advanced Functional Materials, **21**, 2705–2711 (2011). https://doi.org/10.1002/adfm.201100429

[129] Zujovic Z. D., Gizdavic-Nikolaidis M., Kilmartin P. A., Travas-Sejdic J., Cooney R. P., Bowmaker G. A.: Solid-state magnetic resonance studies of polyaniline as a radical scavenger. Applied Magnetic Resonance, **28**, 123–136 (2005). https://doi.org/10.1007/BF03166999

[130] Addiego F., Mihai I., Marti D., Wang K., Toniazzo V., Ruch D.: Polyaniline as potential radical scavenger for ultra-high molecular weight polyethylene. Synthetic Metals, **198**, 196–202 (2014). https://doi.org/10.1016/j.synthmet.2014.10.020

[131] Forrest S. R.: The limits to organic photovoltaic cell efficiency. MRS Bulletin, **30**, 28–32 (2005). https://doi.org/10.1557/mrs2005.5

[132] Bai S., Ma Y., Luo R., Chen A., Li D.: Room temperature triethylamine sensing properties of polyaniline-WO_3 nanocomposites with p-n heterojunctions. RSC Advances, **1**, 2687–2694 (2015). https://doi.org/10.1039/C5RA20843B

[133] Li S., Lin P., Zhao L., Wang C., Liu D., Liu F., Sun P., Liang X., Liu F., Yan X., Gao Y., Lu G.: The room temperature gas sensor based on polyaniline@flower-like WO_3 nanocomposites and flexible PET substrate for NH_3 detection. Sensors and Actuators B: Chemical, **259**, 505–513 (2018). https://doi.org/10.1016/j.snb.2017.11.081

[134] Xu C., Jin K., Xiao Z., Zhao Z., Ma X., Wang X., Li J., Xu W., Zhang S., Ding L., Zhang F.: Wide band gap polymer with narrow photon harvesting in visible light range enables efficient semitransparent organic photovoltaics. Advanced Functional Materials, **31**, 2107934 (2021). https://doi.org/10.1002/adfm.202107934

[135] Xu W., Ma X., Son H. J., Jeong S. Y., Niu L., Xu C., Zhang S., Zhou Z., Gao J., Woo H. Y., Zhang J., Wang J., Zhang F.: Smart ternary strategy in promoting the performance of polymer solar cells based on bulk-heterojunction or layer-by-layer structure. Small, **17**, 2104215 (2021). https://doi.org/10.1002/smll.202104215

[136] Green M. A.: Photovoltaic principles. Physica E: Low-dimensional Systems and Nanostructures, **14**, 11–17 (2002). https://doi.org/10.1016/S1386-9477(02)00354-5

[137] Zhang L., Mohamed H. H., Dillert R., Bahnemann D.: Kinetics and mechanisms of charge transfer processes in photocatalytic systems: A review. Journal of Photochemistry and Photobiology C: Photochemistry Reviews, **13**, 263–276 (2012). https://doi.org/10.1016/j.jphotochemrev.2012.07.002

[138] van der Lubbe S. C. C., Guerra C. F.: The nature of hydrogen bonds: A delineation of the role of different energy components on hydrogen bond strengths and lengths. Chemistry an Asian Journal, **14**, 2760–2769 (2019). https://doi.org/10.1002/asia.201900717

[139] Wolters L. P., Bickelhaupt F. M.: Halogen bonding *versus* hydrogen bonding: A molecular orbital perspective. Chemistry Open, **1**, 96–105 (2012). https://doi.org/10.1002/open.201100015

[140] Wang B., Jiang W., Dai X., Gao Y., Wang Z., Zhang R-Q.: Molecular orbital analysis of the hydrogen bonded water dimer. Scientific Reports, **6**, 22099 (2016). https://doi.org/10.1038/srep22099

[141] Ashassi-Sorkhabi H., Asghari E., Mirmohseni A.: Photovoltaic properties of polyaniline-copoly(butyl acrylate/vinyl acetate) composite. Iranian Polymer Journal, **17**, 711–719 (2008).

[142] Zhao W., Ye L., Zhang S., Fan B., Sun M., Hou J.: Ultrathin polyaniline-based buffer layer for highly efficient polymer solar cells with wide applicability. Scientific Reports, **4**, 6570 (2014). https://doi.org/10.1038/srep06570

[143] Zhang X., Lan Z., Wu J., Lin J., Fan L.: Enhancing photovoltaic performance of photoelectrochemical solar cells with nano-sized ultra thin Sb_2S_3-sensitized layers in photoactive electrodes. Journal of Materials Science: Materials in Electronics, **24**, 1970–1975 (2013). https://doi.org/10.1007/s10854-012-1043-8

[144] Chal P., Shit A., Nandi A. K.: Dye-sensitized solar cell from a new organic n-type semiconductor/polyaniline composite: Insight from impedance spectroscopy. Journal of Materials Chemistry C, **4**, 272–285 (2015). https://doi.org/10.1039/C5TC03072B

[145] Bejbouji H., Vignau L., Miane J. L., Dang M-T., Oualim E. M., Harmouchi M., Mouhsen A.: Polyaniline as a hole injection layer on organic photovoltaic cells. Solar Energy Materials and Solar Cells, **94**, 176–181 (2010). https://doi.org/10.1016/j.solmat.2009.08.018

[146] Vu H. H. T., Hwang Y-H., Kim H-K.: The effects of WO_3 nanoparticles addition to the TiO_2 photoelectrode in dye-sensitized solar cells. Current Photovoltaic Research, **4**, 42–47 (2016). https://doi.org/10.21218/CPR.2016.4.2.042

[147] You Y., Tian W., Min L., Cao F., Deng K., Li L.: TiO_2/WO_3 bilayer as electron transport layer for efficient planar perovskite solar cell with efficiency exceeding 20%. Advanced Materials Interfaces, **7**, 1901406 (2020). https://doi.org/10.1002/admi.201901406

[148] Sakthivel P., Muthukumaran S., Ashokkumar M.: Structural, band gap and photoluminescence behaviour of Mn-doped ZnS quantum dots annealed under Ar atmosphere. Journal of Materials Science: Materials in Electronics, **26**, 1533–1542 (2015). https://doi.org/10.1007/s10854-014-2572-0

[149] Shan F. K., Liu G. X., Lee W. J., Shin B. C.: Stokes shift, blue shift and red shift of ZnO-based thin films deposited by pulsed-laser deposition. Journal of Crystal Growth, **291**, 328–333 (2006). https://doi.org/10.1016/j.jcrysgro.2006.03.036